**Department of Physics and Astronomy**
**University of Heidelberg**

Bachelor Thesis in Physics
submitted by

**Alexander Gresch**

born in Gütersloh (Germany)

**2017**

# The Quasi-momentum in an Experimentally Implemented Quantum Walk

This Bachelor Thesis has been carried out by Alexander Gresch at the
Institute for Theoretical Physics in Heidelberg
under the supervision of
Prof. Dr. Sandro Wimberger

## Abstract

The concept of quantum walks was proposed around 25 years ago and they have become experimentally feasable and controllable in the last ten years. The experimental implementation of a time-discrete quantumn walk studied in this thesis comes with additonal effects which are investigated for a better theoretical understanding of the walk. We consider the two most dominant ones by analytical treatment and via simulations with respect to their impacts on the walk. Because it requires a certain quantum resonance condition we investigate in small experimental deviations from the ideal case from a theoretical viewpoint. The results are compared with recent experimental findings.
The studied effects allow for a better engineering of the implemented quantum walk and are of experimental interest of the quantum walk applications. Experimentally feasible and thus investigated ones are for example a steered walk, its transition to classical behaviour or the reversal of any walk step.



## Zusammenfassung

Obwohl Quantum Walks konzeptionell bereits vor etwa 25 Jahren vorgeschlagen worden sind, können sie erst seit den letzten 10 Jahren experimentell kontrollierbar umgesetzt werden. In dieser Bachelorarbeit beschäftigen wir uns mit der Implementierung eines solchen zeitdiskreten Quantum Walks. Bei jener Umsetzung treten zusätzliche Effekte auf, die für ein tieferes theoretisches Verständnis des Walks untersucht werden. Wir behandeln die zwei hauptsächlichen Effekte. Ihr jeweiliger Einfluss auf den Walk kann sowohl durch eine analytische Beschreibung, als auch durch Computersimulationen erkennbar gemacht werden. Da für den Walk eine bestimmte Quantenresonanz-Bedingung erfüllt sein muss, berücksichtigen wir kleine experimentelle Abweichungen vom Idealfall auf theoretischer Basis. Die Resultate werden anschließend mit neuen experimentellen Daten verglichen.
Ein Verständnis der Einflüsse auf den Walk führt zu einer höheren experimentellen Kontrolle und macht die experimentelle Umsetzung interessant für Anwendungen. Darunter befinden sich der hier untersuchte einseitig gerichtete Walk, ebenso wie dessen Übergang zu klassischem Verhalten oder die Reversibilität des Walks.

# Contents

# 1. Theoretical background

Since the pioneer paper [1] by Aharonov et al. in 1993 where random walks relying on quantum rather than classical properties were introduced there has always been a great interest of research regarding the fact that quantum walks may play a key role in search algorithms run on quantum computers [2]. Using entanglement and superposition as a ressource there are hopes of gaining an exponential speed-up in computation time performing a quantum algorithm over a classical one [3, 4, 5]. However, this hope is questionable. It neglects the fact that for $n$ used qubits the number of imposed gates in order to carry out the algorithm grows exponentially leaving no speed-up for the algorithm.
Even though the proposed walk was initially attributed the property of randomness, this characteristics is misleading in the absence of any noise or decoherence. Since the quantum walks are based on the evolution of the corresponding Schrödinger equation they are completely deterministic. The distinction made nowadays is between continous and time-discrete quantum walks. Randomness can then only be introduced by decoherence or noise. The latter will be used in section 4.2.2 in order to study the transition from pure quantum to classical behaviour.
The experimental proposals and actual implementations range from single- [6, 7, 8, 9] over two- [7, 10, 11] to many-particle [12] walks using (ultracold) atoms [6, 11, 13, 14], photons [15, 9, 10] or ions [7, 8]. They can be conducted in real [6, 9, 11, 13, 14], momentum [16] or phase space [7, 8] using e.g. optical lattices [13, 14] or ion traps [7, 8].The implementation of interest for this thesis stems from a proposal by Summy and Wimberger for a time-discrete quantum walk [16]. Its backbone is the well-studied atom optics kicked rotor (AOKR), whose properties for the walk are explained in the first section, combined with quantum ratchets (explained in section 1.1.3).
The experimental implementation is reviewed in the sections 1.3 - 1.3.3. The walk is, however, affected by small deviations from the quantum resonance which we will consider theoretically in chapter 2. For the resonant walk, an analytical desription was already found in [17] which is reviewed in chapter 3. A comparison between the theory and the experiment, including feasable walk applications, is presented in the chapters 4 & 5.

## 1.1. Atom optics kicked rotor

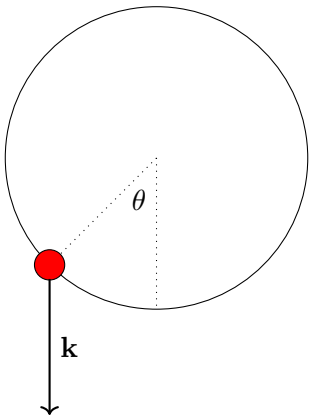


**Figure 1.1.:** Kicked rotor

The AOKR has always been a toymodel for deterministic chaos and a good approximative local description in the energy space for periodically driven systems [18, 19]. Such an example would be the short but periodic interactions in an excited Rydberg atom [20]. A single particle is placed on a rigid ring. At a fixed temporal period a force is applied instantaneously such that its effective strength depends on the particle's position, see fig. 1.1. The circular property can be translated to a rotor on the line with the help of the Bloch theorem; it will be discussed in the next section. The first group to implement an AOKR were the Raizen group from Austin, Texas [21]. Nowadays, Bose-Einstein-condensates (BEC) are used.

The $\delta$-kicked rotor is described by the Hamiltonian (in SI-units) [21]

$$\hat{H}' = \frac{\hat{p}'^2}{2m} + V_0 \cos\big(2k_L\hat{x}'\big) \sum_{z\in\mathbb{Z}} \delta(t' - zT_p) \tag{1.1}$$

with the momentum and position operators $\hat{p}'$ and $\hat{x}'$, particle mass $m$, kicking period $T_p \gg$ kick duration $\Delta T$ with strength (induced by the potential) $V_0$ of a standing laser wave with wave vector $k_L$. For practical purposes, eq. 1.1 is redimensionalized by quantising the position

$$\hat{\theta} = \hat{x}' \mod (2\pi) \tag{1.2}$$

in units of $(2k_L)^{-1}$. The commutator relation $[\hat{x}', \hat{p}'] = i\hbar$ then fixes the momentum in units of $\hbar \cdot (2k_L)$. The mass is not rescaled and therefore in units of $m$ which fixes the energy E to be in units of $\frac{(2\hbar k_L)^2}{m}$. The factor 1/2 is not included to ensure the contravariance of the Hamiltonian. Since time is in units of $\frac{\hbar}{[E]}$, it is rescaled into $\frac{m}{\hbar(2k_L)^2}$ and the kicking period is made dimensionless via $\tau = \frac{T_p}{[T_p]} = \hbar T_p \frac{(2k_L)^2}{m}$, also leaving a dimensionless time $t = \frac{t'}{\tau}$.
The rescaled Hamiltonian now reads

$$\hat{H} = \frac{\hat{p}^2}{2} + k\cos\hat{\theta} \sum_{z\in\mathbb{Z}} \delta(t - z) \tag{1.3}$$

with a rescaled potential $\int_{\Delta T} V_0(t)\, dt \approx \tilde{V_0} \cdot \Delta T$ and a (dimensionless) kicking strength

$$k = \tilde{V_0} \cdot \Delta T \tag{1.4}$$

Of course, a true $\delta$-kick is not implementable in an experiment (hence the pulse duration $\Delta T$), but with a kicking pulse duration of lower than a microsecond compared to kick periods of several dozen microseconds this is a justifiably good approximation.

The time evolution of the system can be obtained by integrating eq. 1.3 over one period and applying it to the Schrödinger equation which yields a unitary time evolution operator

$$\hat{U} = \exp\left(-i \int_t^{t+\tau} H(t')dt'\right) = e^{-\frac{i}{2}\tau\hat{p}^2} e^{-ik\cos\hat{\theta}} \tag{1.5}$$

called the Floquet operator [22]. Due to the $\delta$-like kicking, the operator factorizes into a kicking part and one corresponding to the free evolution of the system between two consecutive kicks after a kick.
As stated earlier, there is a mapping between the rotor on a circle and the atom optic kicked rotor on the line which is of interest for the experiment. It can be formulated with the help of the Bloch theorem in the next section.

### 1.1.1. Bloch theorem

As seen in eq. 1.2 the periodicity of the potential implies spatial periodic boundaries. For these potentials the Bloch theorem states that the corresponding stationary Schrödinger equation is composed of a coherent superposition of all basis solutions such that the wave function in position space corresponds to

$$\psi(x) = e^{i\beta x}\psi_\beta(x) \tag{1.6}$$

where $\psi_\beta(x)$ is a $2\pi$-periodic function just like the potential. The theorem also implies that momenta can only be altered by integer values while conserving the non-integer part that is called the quasi-momentum $\beta$. The total momentum $p$ can thus be split into

$$\hat{p} = \hat{n} + \beta \tag{1.7}$$

where $n$ is the integer momentum class und $\beta \in [0, 1)$ is the conserved fractional quasi-momentum. The integer momenta $n$ are the eigenvalues to the angular momentum operator

$$\hat{n} = -i\frac{\partial}{\partial\theta} \tag{1.8}$$

The generell solution will then be a coherent superposition of all Bloch waves, the so called Bloch fibration, with a quasi-momentum distribution $\rho(\beta)$

$$\Psi(x) = \int_0^1 \mathrm{d}\beta\rho(\beta)e^{i\beta x}\psi_\beta(x) \tag{1.9}$$

As it can be seen in eq. 4.6 we will not treat the coherent superposition but rather assume that each particle contributes its own (conserved) quasi-momentum to the BEC ensemble. A very similar result to the coherent superposition is obtained when averaging classically over all contributing particles in the BEC. A comprehensive discussion can be found in [20, 23]. The Bloch wave describing each initialisation $p_0 = n_0 + \beta_0$ is therefore

$$\psi_\beta(\theta) = \langle\theta|\psi_\beta\rangle = \frac{1}{\sqrt{2\pi}} e^{in_0\theta} \tag{1.10}$$

$$\rho(\beta) = \delta(\beta - \beta_0) \tag{1.11}$$

Substituting eq. 1.7 in eq. 1.5 finally yields

$$\hat{U} = e^{-\frac{i}{2}\tau(\hat{n}+\beta)^2} e^{-ik\cos\hat{\theta}} \tag{1.12}$$

in the most general form. Interesting behaviour however arises for specific values of quasi-momentum and kick durations. These are called quantum resonances and treated in the next section.

### 1.1.2. Quantum resonance

Interesting behaviour is found for specific values for the kick period $\tau$ and the quasimomentum which are referred to as quantum resonance of the atomic optics kicked rotor [24]. For these resonances the free evolution only contributes a global phase which can be dropped as we are solemnly interested in the momentum distribution. This means that during the free evolution the system evolves back into the state it started evolving from and thus it cannot be distinguished between $T$ kicks with strength $k$ and a single one with strength $kT$. Expressing

$$\tau = 2\pi l \qquad\qquad l \in \mathbb{N} \tag{1.13}$$

$$\beta = \frac{1}{2} + \frac{i}{l} \mod 1 \qquad\qquad i = 0, 1, \ldots, l-1 \tag{1.14}$$

gives a criterion for period and corresponding (resonant) quasimomentum. The periods $2\pi$ ($l = 1$) and $4\pi$ ($l = 2$) can be viewed as half and full Talbot time respectively, now only in a temporal domain [22]. We will focus on experiments tuned into the full Talbot time later on in section 1.3
Another ansatz investigated in [23] is defining $\xi = \pi l(2\beta \pm 1) \mod 2\pi$ which simplifies eq. 1.12 into

$$\hat{U}_\xi = e^{-i\xi\hat{n}} e^{-ik\cos\hat{\theta}} \tag{1.15}$$

A single application, i.e. one walk step, is now equivalent to the mapping $\psi_\beta(\theta, t = 0) \mapsto \psi_\beta(\theta - \xi, t = 1)$ and the quasimomentum can be interpreted as a rotation in the periodic spatial domain. In [23] the momentum distribution of the initial state in eq. 1.10 was

calculated to be

$$P(n, T; n_0, \beta_0, k) = J^2_{n-n_0}(|W_T|) \tag{1.16}$$

with $J$ being the Bessel function of the first kind. A brief overview about Bessel functions of the first kind and some useful relations can be found in appendix A. The argument of the Bessel function is evaluated to be

$$W_T = kT \qquad \text{for } \xi = 0 \tag{1.17}$$

$$W_T = k\left|\frac{\sin\left(\frac{T\xi}{2}\right)}{\sin\left(\frac{\xi}{2}\right)}\right| \qquad \text{for } \xi \neq 0 \tag{1.18}$$

In the resonant case $\xi \equiv 0$ a linear energy growth over time within the kicked system (i.e. ballistic motion) is expected. This fundamentally differs from classical diffusion phenomena having an energy growing with $\sqrt{t}$ which makes the quantum resonant case possibly useful for novel quantum algorithms. We note a formula similar to eqs. 1.17 & 1.18 to be found in the experimental walk implementation (compare eqs. 2.31 & 2.32).

### 1.1.3. Quantum ratchets

Ratchets in a classical sense refer to a directed transport due to a biased potential. A prominent example would be the toothsaw potential [25] where particles are confined at grid positions yet with a tilt to one of the neighbouring grid positions. Turning off the potential for a short evolution time and on again will result in a mean transport of particles to the preferred direction induced by the potential.

In the quantum case - as the potential is symmetric in position space - the symmetry is broken by the initial state itself and not the potential [26, 27, 28]. This can be realized by an initial choice of two adjacent momentum classes but breaking the spatial symmetry with a relative phase. Such a ground state would be

$$|\psi(\phi)\rangle = \frac{1}{\sqrt{2}}\Big(|n=0\rangle + e^{i\phi}\,|n=1\rangle\Big) \tag{1.19}$$

This state is symmetric around momentum $p = 1/2$ now and breaks the spatial symmetry for $\phi \neq 0, \pi$. A rigorous calculation [22, 29] yields for the change in mean momentum

$$\langle p\rangle_{T+1} - \langle p\rangle_T = -\frac{k}{2}\sin\phi \tag{1.20}$$

Thus for the initialised state in the experimental section 1.3 where $\phi = \pm\frac{\pi}{2}$ and $k \approx 2$ this would correspond to a mean momentum shift of $\mp 1$ respectively.

## 1.2. Time-discrete quantum walk

The quantum walks are the quantum counter parts to classical random walks that are widely used in computer science (e.g. search algorithms), observed in biology (e.g. cell diffusion) and further sciences [30]. For a comprehensive overview we refer to [31] by Kempe.
As already mentioned it is distinguished between continuous and time-discrete quantum walks, here we will investigate the latter. In a classical walk on the line the walker will flip a coin which determines its direction taken for the following step. Repeating this walk a multitude of times we classically expect the grid position distribution to trend towards a Gaussian (as the limit from the binomial distribution). In the quantum case, each step is a superposition of going left and right at the same time. This is achieved by two different internal states (such as the two spin states $|\uparrow\rangle$ & $|\downarrow\rangle$ for example) which determine the walk direction, opposite to each other. This internal state will act as a 'coin' for the walk direction on the external level (such as position or momentum space). Such a walk step can be represented with the following unitary shift operator

$$\hat{T} = \sum_i \Big[ |\downarrow\rangle\langle\downarrow| \otimes |i\rangle\langle i-1| + |\uparrow\rangle\langle\uparrow| \otimes |i\rangle\langle i+1| \Big] \tag{1.21}$$

The shift operator thus entangles the two degrees of freedom. If the walker starts in a symmetric state in the internal level, a walk driven by eq. 1.21 will correspond to simultanously walking to the left and right in the external level. In order to garantuee such a superposition, the internal levels have to be mixed with each other using a so called balanced coin. The often used Hadamard coin

$$\hat{C}_{Had} = \frac{1}{\sqrt{2}} \begin{pmatrix} 1 & 1 \\ -1 & 1 \end{pmatrix} \tag{1.22}$$

would be such a balanced one. After the initialisation the two internal levels have to be seperated from each other during the mixing. This can be done by e.g. initialising with the Hadamard coin (eq. 1.22) and mixing with

$$\hat{C}_{walk} = \frac{1}{\sqrt{2}} \begin{pmatrix} 1 & i \\ i & 1 \end{pmatrix} \tag{1.23}$$

which is still a balanced coin. However, the two internal levels are now kept from each other by seperating one into the imaginary domain [31]. The schematic of this walk procedure is depicted in fig. 1.2. Red, filled grid positions correspond to populated ones whereas the adjacent, unfilled ones are not reached by the walk at the same walk step. This is a feature of the shift operator in eq. 1.21 which moves all walkers from odd to even grid positions and vice versa. If it is started for example at an even grid position the next step will only have non-zero probabilities at odd grid positons.

It is now quite peculiar how two walkers interfere with each other when they come from different grid positions to the same one. In the case of the unitary shift operator in

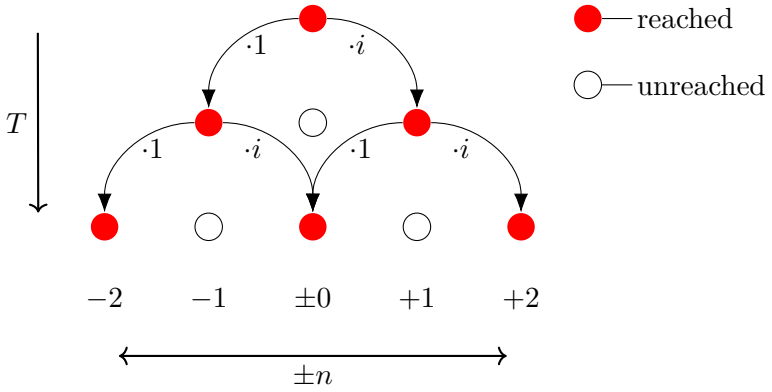


**Figure 1.2.:** A scheme of the quantum walk using the shift operator (eq. 1.21) and starting in a single arbitrary momentum class (upper row). Each row corresponds to the following walk step. Only the exactly adjacent momentum classes are reached (red circles). The phase gain due to the mixing with eq. 1.23 is indicated at each transition.

eq. 1.21 most of the walkers around the centre positions (from where the walk started) will interfere destructively leaving only a small final momentum distribution which was proven to approach a uniform shape [32]. Therefore the momentum distribution will mainly have two distinctive peaks spreading further away from the starting point, see fig. 1.3. This corresponding walker initialisation used eq. 1.19 with a phase of $-\pi/2$ and the Hadamard coin in eq. 1.22. The momentum distributions for 50 (blue with $\cdot$ on the lines) and 100 (green with $\times$ on the lines) are shown, demonstrating the linear spread. For that the respective grid position of the maximal probability is drawn with dashed lines. It doubles for twice the walk steps implying ballistic motion. We note that the distinctive peak feature can be enhanced by an initial state choice that consists of more momentum classes [33, 34, 35].

Whereas the distribution converges to a Gaussian shape in the classical walk, the quantum walk in resonance does not have such a feature due to the ballistic motion. As it will be demonstrated in section 2.1, the symmetry of the walk depends on the initial and mixing coin chosen.

The AOKR Hamiltonian in eq. 1.3 can feature the needed grid shift in eq. 1.21 if seen as a walk in momentum and not position space. It corresponds to a unitary operator shifting the external level either left or right when in quantum resonance. What is missing there is the internal level structure needed for the coin toss. In the next section we will have a closer look on how to experimentally implement both the shift operator (in both possible directions) and the mixing of the internal levels.

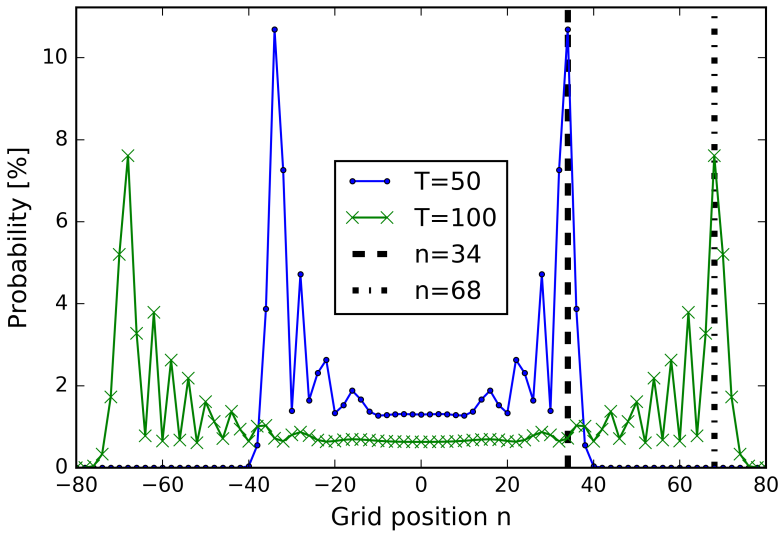


**Figure 1.3.:** Grid probability for the quantum walk using eq. 1.21 and eqs. 1.22 & 1.23 as initialisation and walk coin respectively. The walk starts at grid position 0 and 1 according to eq. 1.19 and the number of kicks is $T = 50, 100$ to demonstrate the ballistic motion. The grid positions of the respective (right-wing) maxima are also indicated for that purpose.

## 1.3. Experimental set-up

The experiment uses an ultracold $^{87}$Rb Bose-Einstein-condensate (BEC) which is trapped in an optical lattice created by a standing wave laser. A scheme of the set-up is given in fig. 1.4. The BEC is created using evaporative cooling techniques and trapped by a focused $CO_2$ laser beam. The preparation eventually leaves roughly 70,000 Rb atoms in the condensate. Details on cooling methods or the used magneto-optical trap can be found elsewhere [36].

In this set-up the external degree of freedom corresponds to the centre of motion momentum of the BEC. After releasing the ultracold atoms from the trap a sequence of kicks is applied by the optical lattice. The counterpropagating laser beams making up the standing wave are tuned half way between the energies of the internal hyperfine levels at $\lambda \approx 780nm$. Deviating from fig. 1.4 the two lasers are aligned with a relative angle of 53° to each other corresponding to a spatial period of $\lambda_G = \lambda/(2\sin(53°))$. As mentioned earlier in 1.1.2 we work at full Talbot time giving $\tau = 103\mu s$. The ac-Stark shift for the internal levels then differs in sign leaving a positive or negative kicking strength

$$k = \frac{\Omega\tau_{pulse}}{\Delta} \tag{1.24}$$

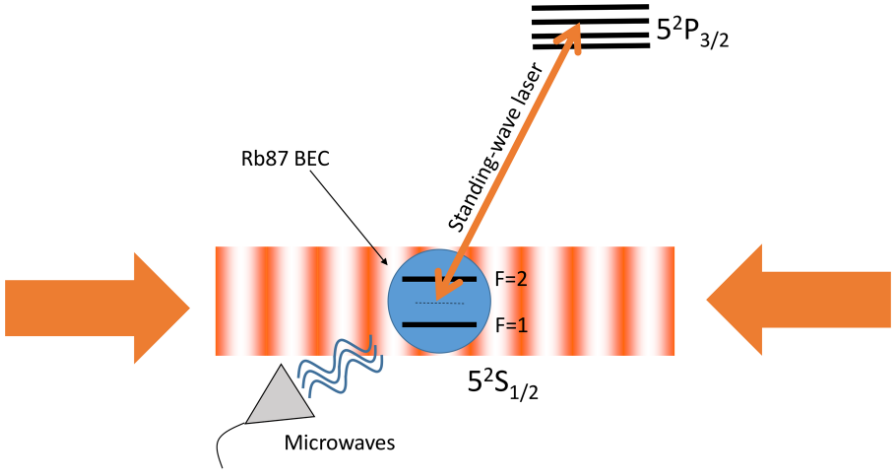


**Figure 1.4.:** Scheme of the experimental set-up of the quantum walk. A sequence of kicks is applied on a BEC at quantum resonance by a pulsed optical lattice. The internal hyperfine levels of $^{87}$ Rb can be adressed by microwaves. Taken from [16].

with a Rabi frequency $\Omega$, pulse duration $\tau_{pulse} \approx 380ns \ll \tau$ (the so-called Raman-Nath regime) and respective detuning from the internal levels $\Delta$. With eq. 1.20 this gives two ratchet currents in opposite directions.
For these internal levels, the hyperfine levels of Rb (being a pseudospin $\pm 1/2$ system whose configurations we note with $|F=2\rangle \equiv |\uparrow\rangle$ and $|F=1\rangle \equiv |\downarrow\rangle$) will serve as a governour for the coin flip and hence the walk direction. The mixing between both levels is achieved by microwaves and can be represented with the unitary rotation matrix

$$\hat{M}(\alpha,\chi) = \begin{pmatrix} \cos\frac{\alpha}{2} & e^{-i\chi}\sin\frac{\alpha}{2} \\ -e^{i\chi}\sin\frac{\alpha}{2} & \cos\frac{\alpha}{2} \end{pmatrix} \tag{1.25}$$

where $\alpha = \Omega\tau$ (this means a constantly active radiation. But due to the Raman-Nath regime the influence during the kick is negligible and afterwards uncoupled to the free evolution; i.e. the instantenous form of eq. 1.25 is justified) and $\chi$ is a phase tunable by an acusto-optical modulator. This way it is straight-forward to implement eqs. 1.22 & 1.23. The state initialisation is realized by applying an off-resonant Bragg pulse [19] (with the correct phase $-\pi/2$) onto $|n=0\rangle \otimes |\downarrow\rangle$ and applying the Hadamard gate:

$$|n=0\rangle \otimes |\downarrow\rangle \overset{Bragg}{\mapsto} \frac{|n=0\rangle - i\,|n=1\rangle}{\sqrt{2}} \otimes |\downarrow\rangle \tag{1.26}$$

$$\overset{\hat{C}_{Had}}{\mapsto} \frac{|n=0\rangle - i\,|n=1\rangle}{\sqrt{2}} \otimes \frac{|\uparrow\rangle + |\downarrow\rangle}{\sqrt{2}} \tag{1.27}$$

The whole scheme is shown in fig. 1.5.
The final momentum distribution is obtained by time-of-flight imaging. For that the atoms are released from the lattice and will expand under gravity and their momentum

until they are exposed to near-resonant light. The following flourescence is captured by a CCD-camera and reconverted into the momentum distribution.

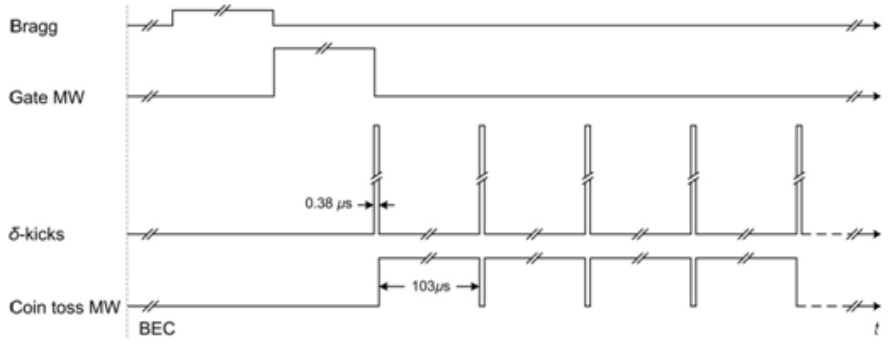


**Figure 1.5.:** Representation of the experimental protocoll. The Bragg pulse and the gate microwave initialise the wave function which is then exposed to the kicking sequence. Time-of-flight imaging afterwards not shown here. Taken from [37].

### 1.3.1. The time step operator in quantum resonance

At quantum resonance the free evolution part of the Floquet operator vanishes. Thus, a kicking sequence then consists of the actual kick (denoted by the operator $\hat{K}$) and a mixing $\hat{M}$ of the internal two levels. We will use $\alpha = \frac{\pi}{2}$ and $\chi = -\frac{\pi}{2}$, resulting in eq. 1.23. The kick is done via

$$\hat{K} = \exp\Big(-ik\cos\hat{\theta}\cdot\sigma_z\Big) = \begin{pmatrix} e^{-ik\cos\hat{\theta}} & 0 \\ 0 & e^{ik\cos\hat{\theta}} \end{pmatrix} \tag{1.28}$$

where $\sigma_z$ is the third Pauli matrix. This leads to

$$\hat{U}_{kick} = \hat{M}\hat{U} = \frac{1}{\sqrt{2}}\begin{pmatrix} e^{-ik\cos\hat{\theta}} & ie^{ik\cos\hat{\theta}} \\ ie^{-ik\cos\hat{\theta}} & e^{ik\cos\hat{\theta}} \end{pmatrix} \tag{1.29}$$

for single walk step. A walk with $T$ steps is therefore described via $\hat{U}^T_{kick}$.

### 1.3.2. Elimination of the phase $\Phi$ in the kicking matrix

A rigorous treatment [20, 17] of the system reveals two phases, treating the two levels differently from each other. One is induced by the energy difference of the the two levels, the other comes from the conversion of $\cos^2(x) = \frac{1}{2}(\cos(2x)+1)$ since the quantum mechanical treatment of the effective two-level system yields the square and not the desired cosine. Both add up to an effective phase $\Phi$ altering eq. 1.28 into

$$\begin{pmatrix} e^{-ik\cos\hat{\theta}} & 0 \\ 0 & e^{ik\cos\hat{\theta}}\cdot e^{i\Phi} \end{pmatrix} \tag{1.30}$$

It is easy to show that

$$\hat{M}(\pi, 0) \cdot \hat{M}(\pi, \Phi/2) = -e^{i\frac{\Phi}{2}} \cdot \mathbb{1} \tag{1.31}$$

Application of the two pulses before each kick leads to a proper removal of the phase, leaving only a global one which has no effect on the overall probability distribution.

The BEC however has a small momentum width around the integer values $n$ - due to Heisenberg's uncertainty principle - which is assumed to be Gaussian [38] with mean of 0 (the resonant case) and some full width half maximum $\beta_{FWHM}$. Including this into the theoretical treatment of the system could be achieved for the AOKR [23] but not yet for the quantum walk present in the experiment. Due to entanglement of the two degrees of freedom the same method as applied for the AOKR could not be repeated. However, by reformulating the Floquet operator in eq. 1.12 a similar result could be obtained in chapter 2.
A full analytical description of the resonant case is already given in [17] which is shortly presented in chapter 3 and compared to the new theory in the limit $\beta \to 0$.

### 1.3.3. Experimental limitations

There are three main aspects in the experiment that limit the implementation for high kick numbers $T$. Firstly, in the experimental data (see chapter 4) there is always a Gaussian peak around the centre of the walk (i.e. its starting point) even for small and intermediate step numbers. This is the effect of the thermal cloud surrounding the BEC but not responding to the optical pulses. In this cloud there is a wide range in quasimomenta (contrary to the ideal walk in resonance) which mostly are off-resonant and thus not responding to the kicking scheme. This always leaves a Gaussian peak, centred around 0, in the momentum distribution for all time steps.
The second effect arises from near-resonant quasimomenta which are considered in chapter 2. Their momentum distributions only follow the resonant one up to a few steps until the induced dephasing gets so strong that the momentum distribution freezes into a Gaussian and is not altered by the kicking afterwards.
The last investigated effect is spontaneous emission (SE) which decoherently destroys the walk spread approaching a Gaussian momentum distribution and thus classical behaviour at higher walk steps. A master equation treatment for the SE was already developed in [17]. Simulations involving the SE using a so called quantum jump method [39] showed a negligible effect. Since the per kick probability was estimated to be less than one percent the effect only becomes significant after over 20 kicks and is therefore experimentally negligible for the experiment going maximally up to 20 kicks at the moment.

# 2. Including the off-resonant quasi-momentum $\beta$

In this chapter, we derive an analytical expression for the momentum distribution that depends on the quasi-momentum $\beta$ of a single particle. There is a close relation to the structure of a Galton board on which the quantum walk takes place [31] due to the relation between the unitary shift operator and the kicking part of eq. 1.28. For the quantum resonance limit $\beta \to 0$, an analytical expression for the momentum distributions was already found in [17]. Its derivation is reviewed in chapter 3. As shown in section 4.2.1, the two theories predict the same outcome for every single walk step in resonance. Therefore, the theory developed in section 2.3 extends the calculations of [17] to arbitrary quasi-momenta but with an approximative constraint.
Preceeding the calculations however, we have a closer look on how the walk symmetry is related to the choice of coins for the initialisation and the mixing of the internal levels. The relation is illustrated in the following section 2.1.

## 2.1. The symmetry of the walk with respect to the coin choice

This section is meant to illustrate how the choice of the coins for initialisation and mixing between consecutive steps effects the symmetry of the corresponding momentum distribution. This really is a feature of the coins acting on the internal levels only and independent from the external state. As mentioned already in section 1.2, the symmetry is only obtained for different coins such as eqs. 1.22 & 1.23. The relation between the experimentally used kicking matrix $\hat{K}$ and the shift operator $\hat{T}$ (eqs. 1.29) & 1.21 respectively) is given in the next section 2.2 and we therefore demonstrate the effect of the coin choice for the walk driven by $\hat{T}$ e.g. in fig. 1.3.
For better illustration we will only consider a plane wave in position space and therfore choose an arbitrary initial state of $|n=0\rangle \otimes |\downarrow\rangle$. This is the experimental state without the application of the Bragg-pulse in eq. 1.26 and is mixed by the Hadamard coin in eq. 1.22. We can now either choose the same coin $\hat{C}_{Had}$ or the walk coin $\hat{C}_{walk}$ for all the following mixings.
This yields

$$|0\rangle \otimes \frac{|\uparrow\rangle + |\downarrow\rangle}{\sqrt{2}} \overset{\hat{C}_{walk}\circ\hat{T}}{\mapsto} \frac{1+i}{2}\Big[\,|1\rangle \otimes |\uparrow\rangle + |-1\rangle \otimes |\downarrow\rangle\,\Big] \tag{2.1}$$

$$|0\rangle \otimes \frac{|\uparrow\rangle + |\downarrow\rangle}{\sqrt{2}} \overset{\hat{C}_{Had}\circ\hat{T}}{\mapsto} i\,|1\rangle \otimes |\uparrow\rangle \tag{2.2}$$

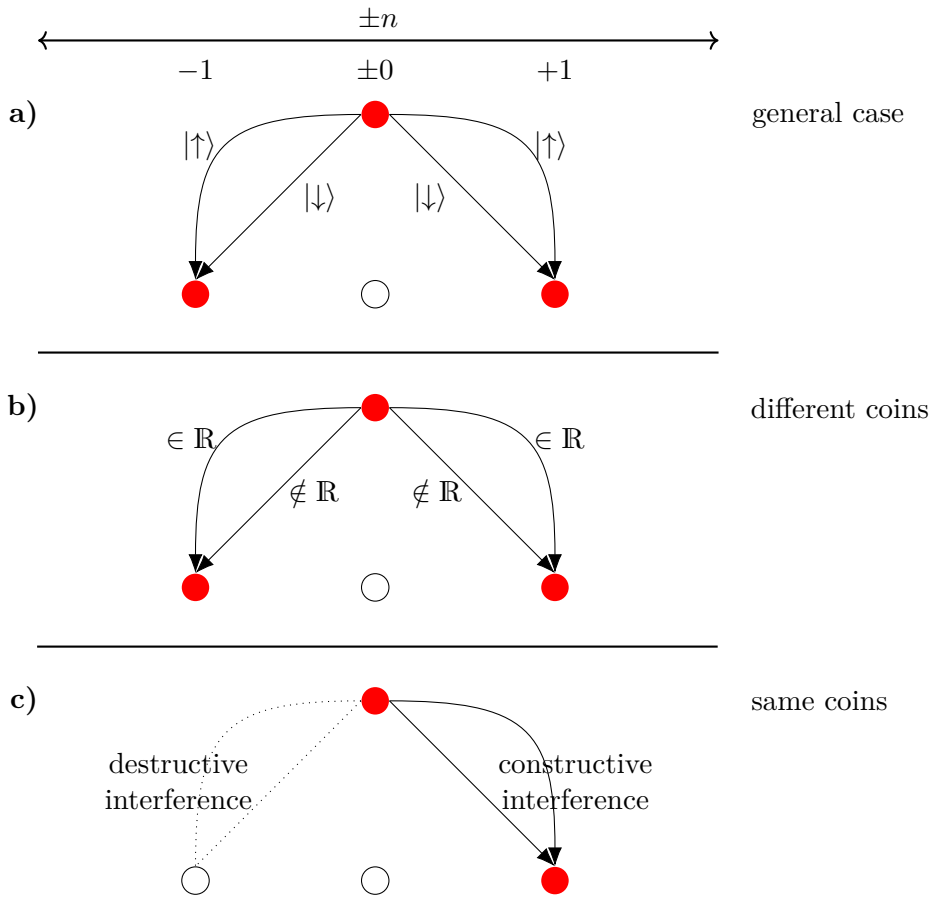


**Figure 2.1.:** Comparison of how the coin choice affects the walk symmetry. The first step (a) shows generally how the walker moves from a specific momentum class (first row) to the exactly adjacent ones during one walk step. Due to the mixing both internal levels will effect the momentum class population. For different balanced coins (b) one internal level will give a real contribution whereas the other level solely contributes an imaginary part and thus the two internal level contributions cannot interfere with each other. This is different if the same coin is chosen for initialisation as well as for the walk (c). Depending on the relative phases within the coins the level contributions interfere either constructively or destructively. This results in a net momentum flux during this walk step and thus breaks the existing symmetry of the momentum distribution.

Whereas a different coin (with a phase difference in the off-diagonal elements) results in a symmetric momentum probability around $n = 0$, using the same coin for the walk produces a mean momentum change. As a consequence, the momentum distribution is now symmetric around $n = 1$. The walk simultaneously propagates to the adjacent momentum classes in each internal level with a specific phase. The mixing recombines the two levels and the wavefunctions for the external level may interfere with each other. This is illustrated in fig. 2.1. Case a) shows the four possible pathways during one step

in general. Due to the mixing of the levels there a two possible paths to each adjacent site. The previous grid position is now unpopulated due to the structure of eq. 1.21. The two paths may now interfere with each other.
In the case of a differently chosen coin from the Hadamard coin in b), the path amplitudes are seperated from each other by keeping one amplitude purely real and the other purely imaginary. No interference can happen in this first step then. If the same coin is chosen for the walk in c), the minus sign in eq. 1.22 leads to destructive interference in one direction and constructive one in the other. It is also interesting to note that the next walk step is equivalent to a new initialisation and thus the second next walk step will again shift the mean momentum by one integer.
The direction of the momentum shift can also be inverted by initialising the state in the other internal level, i.e. $|\uparrow\rangle$.

## 2.2. Reformulating the kicking operator

The free evolution part of the Floquet operator in eq. 1.12 can be examined further by splitting the momentum $p$ into an integer part $n$ and the missing quasi-momentum $\beta$. It follows

$$\begin{aligned} e^{-i\tau\frac{\hat{p}^2}{2}} &= e^{-i\tau\frac{\beta^2}{2}} e^{-i\tau\frac{\hat{n}^2}{2}} e^{-i\tau\beta\hat{n}} && (2.3)\\ &\mapsto \underbrace{e^{-i\tau\frac{\hat{n}}{2}}}_{=1 \text{ for } \tau=4\pi} e^{-i\tau\beta\hat{n}} && (2.4)\\ &= e^{-i\tau\beta\hat{n}} && (2.5) \end{aligned}$$

where the phase could be dropped in the second step as it does not contribute to the final momentum distribution in our apprximation of single $\beta$-trajectories (see discussion around eq. 1.9).
An important relation being used [40] will be

$$\begin{aligned} e^{\pm ik\cos\hat{\theta}} &= \sum_m i^m J_m(\pm k) e^{im\hat{\theta}} \\ &= \sum_m (\pm i)^m J_m(k) e^{im\hat{\theta}} \end{aligned} \tag{2.6}$$

with $J_m$ the Bessel function of the first kind and order $m$. This is the mentioned relation between the experiment and the shift operator in eq. 1.21. Each kick can be interpreted as a weighted sum of infinitely but countably many shift operators connecting the momentum classes $l$ and $n$ with an amplitude of $i^{n-l}J_{n-l}(k)$. Fig. 2.2 gives a comparison between one walk step using the shift operator in a) with the kicking operator expressed in eq. 2.6 in b).

Obviously, the two operators acting during a single kick are in different bases. Mo-

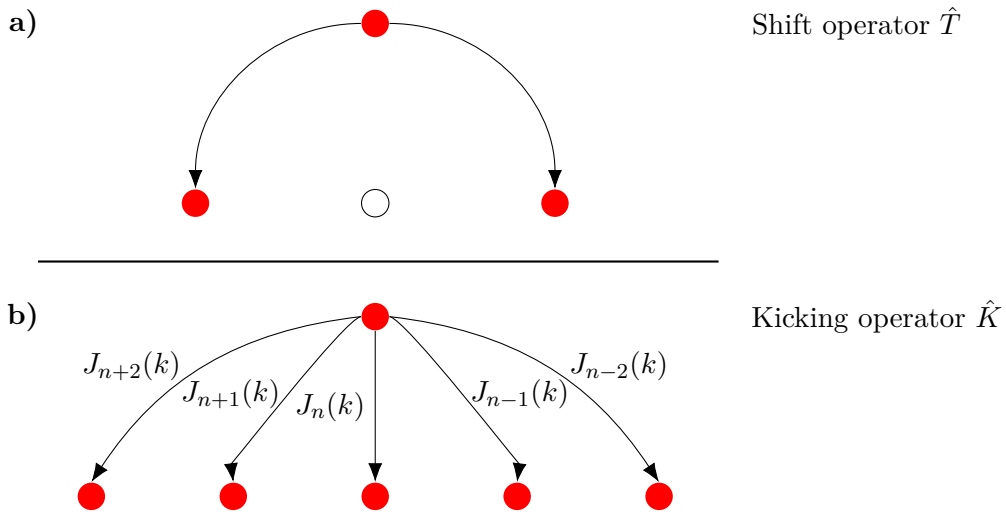


**Figure 2.2.:** The comparison between the quantum walk using the shift operator $\hat{T}$ which only couples adjacent momentum classes (a) with the experimentally implemented quantum walk relying on the kicking operator $\hat{K}$ (b). In this case each momentum class $|n\rangle$ is coupled with every other momentum class $|m\rangle$ with weight $J_{n-m}(k)$.

mentum $n$ and position $\theta$ are however connected via

$$|n\rangle = \frac{e^{in\theta}}{\sqrt{2\pi}} |\theta\rangle \tag{2.7}$$

making the shift operator in the kicking operator expressible in momentum space:

$$e^{\pm im\hat{\theta}} |n\rangle = \frac{e^{in\theta}}{\sqrt{2\pi}} e^{\pm im\hat{\theta}} |\theta\rangle = \frac{e^{i(n\pm m)\theta}}{\sqrt{2\pi}} |\theta\rangle \tag{2.8}$$

$$= |n \pm m\rangle = \sum_j |j \pm m\rangle \langle j|n\rangle \tag{2.9}$$

$$\text{meaning} \quad e^{\pm im\hat{\theta}} = \sum_j |j \pm m\rangle\langle j| \tag{2.10}$$

This explains the name as it shifts particles being in the momentum state $n$ by $\pm m$ momentum classes. As a consequence eq. 2.6 can be understood as an effective coupling of any momentum class with all (adjacent) ones with a weight given by the Bessel function of the first kind, $J_m(\pm k)$ where $m$ is the length of the coupling. This differs a bit from the shift operator in eq. 1.21 where only next neighbours were connected but - however with decreasing weight - a coupling to all other classes (and the same meaning staying at the current momentum class) is made.

In the next chapter we decompose the two Floquet components in the above fashion. Furthermore, we transform the position shift operator into momentum space.

## 2.3. Successive application of the kicking operator $\hat{U}_{kick}$

A single kicking sequence consists of three steps: the $\delta$-kick $\hat{K}$ itself, following free evolution $\hat{F}$ and finally a mixing of the internal states via $\hat{C}_{walk}$. As shown in appendix B, a recurrence relation for the matrix element of the $T$-time application of the kicking sequence is given by

$$\begin{aligned}\hat{U}_{kick}^{T} =& \left(\hat{C}_{walk}\cdot\hat{F}\cdot\hat{K}\right)^{T} \\ =& \frac{1}{\sqrt{2}^{T}}\sum_{m_1,\ldots,m_T} i^{\sum_{i=1}^{T} m_i}\left(\prod_{i=1}^{T} J_{m_i}(k)\right) \\ & \times\sum_{j} e^{-i\tau\beta\left(Tj+\sum_{i=1}^{T}(T+1-i)m_i\right)}\left|j+\sum_{i=1}^{T} m_i\right\rangle\!\left\langle j\right| RM_T\end{aligned} \tag{2.11}$$

where $RM_T = RM_T\left(m_1,\ldots,m_T\right)$ denotes a recurrent $2\times 2$ matrix whose elements have the form of

$$RM_T = \begin{pmatrix} (-1)^{m_1}\left[A_T-1\right] & i\left[B_T+1\right] \\ i(-1)^{m_1}\left[\tilde{A}_T+1\right] & -\left[\tilde{B}_T-1\right]\end{pmatrix} \tag{2.12}$$

The variables $A_T,\ldots$ depend on the values of $\{m_2,\ldots,m_T\}$ due to the mixing of the internal levels. Their recurrence relation can be calculated to be

$$\begin{aligned} A_{T+1} &= (-1)^{m_{T+1}}A_T - (-1)^{m_{T+1}} - \tilde{A}_T & \qquad B_{T+1} &= (-1)^{m_{T+1}}B_T + (-1)^{m_{T+1}} - \tilde{B}_T \\ \tilde{A}_{T+1} &= (-1)^{m_{T+1}}A_T - (-1)^{m_{T+1}} + \tilde{A}_T & \qquad \tilde{B}_{T+1} &= (-1)^{m_{T+1}}B_T + (-1)^{m_{T+1}} + \tilde{B}_T \end{aligned} \tag{2.13}$$

The recurrence start values[1] are found to be

$$A_1 = 2, \quad \tilde{A}_1 = 0, \quad B_1 = 0, \quad \tilde{B}_1 = 0 \tag{2.14}$$

## 2.4. Calculating the matrix elements

The initial state in momentum space is prepared to be

$$\left|\varphi_0\right\rangle = \frac{1}{N}\sum_{l}(-i)^{l}\left|l\right\rangle\otimes\left(\left|\uparrow\right\rangle+\left|\downarrow\right\rangle\right) \tag{2.15}$$

[1] Due the structure of eq. B.10, this form of matrix and thus the recurrence is only valid for $T>0$. The case for $T=0$ is however trivial: $RM_0 = \mathbb{1}$, the identity.

where $\{l\}$ are the prepared momentum classes and $N$ the normalization factor. In this particular case $N = \sqrt{2 \cdot \#l}$ with $\#l$ the number of initialized classes.
The momentum probability distribution is the absolute square of the matrix elements, ending with a particular momentum $n$ and in one of the two internal levels, $|\uparrow\rangle$ and $|\downarrow\rangle$:

$$P(n;T,k,\beta) = \left|\left\langle n\uparrow\middle|\hat{U}_{kick}^{T}\middle|\varphi_0\right\rangle\right|^2 + \left|\left\langle n\downarrow\middle|\hat{U}_{kick}^{T}\middle|\varphi_0\right\rangle\right|^2 \tag{2.16}$$

The former summand is calculated step-wise in the appendix and the later one follows the calculations analogously.
For $T = 1$ this gives

$$\left|\left\langle n\uparrow\middle|\hat{U}_{kick}\middle|\varphi_0\right\rangle\right|^2 = \frac{1}{2N^2}\left|\sum_l (-1)^l \left[J_{n-l}(-k) + iJ_{n-l}(k)\right]\right|^2 \tag{2.17}$$

$$\left|\left\langle n\downarrow\middle|\hat{U}_{kick}\middle|\varphi_0\right\rangle\right|^2 = \frac{1}{2N^2}\left|\sum_l (-1)^l \left[iJ_{n-l}(-k) + J_{n-l}(k)\right]\right|^2 \tag{2.18}$$

The joint probability for the first kick does not depend on the quasi-momentum $\beta$: as the free evolution only contributes a dephasing between two consecuting kicks, here it solely gives a global phase on the matrix elements for a single kick which vanishes by taking the absolute value.
The two kick directions with a respective strength of $k$ and $-k$ can be easily identified and are separated from each other via splitting into a real and imaginary part respectively.
For higher kick counts, e.g. $T = 2$ it is straight-forward to arrive at

$$\begin{aligned}\left\langle n\uparrow\middle|\hat{U}_{kick}^{2}\middle|\varphi_0\right\rangle =& \frac{i^n e^{-i\tau\beta n}}{2N}\sum_l (-1)^l e^{-i\tau\beta l} \\ &\times \sum_{m_1} (*\uparrow)_2 \Big|_{\substack{m_2= \\ n-l-m_1}} J_{m_1}(k) J_{n-l-m_1}(k) e^{-i\tau\beta m_1}\end{aligned} \tag{2.19}$$

with $(*)_2$ being the sum of the upper two entries of the $RM_2$ matrix and shortened for simplicity.
The idea is to use an addition rule for the two intertwined Bessel functions (note their respective indices), namely:

$$J_n(y+z) = \sum_{r\in\mathbb{Z}} J_r(z) J_{n-r}(y) \tag{2.20}$$

Since $(*)_2$ only contains summands of the order $(-1)^x$, they can be contained in the Bessel functions by only adding a minus sign for the argument. The only interfering term here is $e^{-i\tau\beta m_1}$. An *approximation* will be made following the characteristics of

Bessel functions with complex arguments [41]

$$e^{ln\pi i} J_n(z) = J_n\left(z \cdot e^{l\pi i}\right) \qquad l \in \mathbb{Z} \tag{2.21}$$

that - since $\beta$ is significantly small - above eq. 2.21 still holds true for values $l$ close to being an integer. The approximation is justified for almost all $n$ except 0 and 1, as can be seen in fig. 2.3.

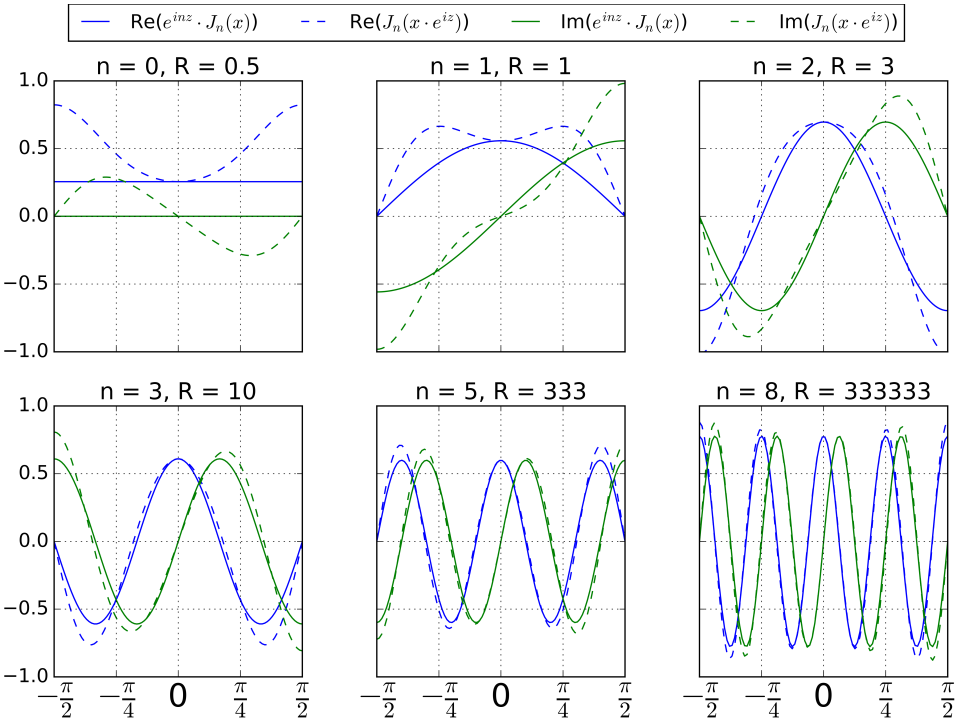


**Figure 2.3.:** Real and imaginary part of the function and its approximation. For better visibility of the accordance for higher $n$, the functions were rescaled in height to be comparable with each other, i.e. each of the four graphs per box was multiplied with the factor $R$ in the title for comparable plots.

The impact on the probability distribution will be discussed later on.

The approximation results in

$$\left|\left\langle n\uparrow\left|\hat{U}_{kick}^2\right|\varphi_0\right\rangle\right|^2 \approx \frac{1}{4N^2}\Bigg|\sum_l (-1)^l e^{-i\tau\beta l}\left(J_{n-l}\left[-k\left(1+e^{-i\tau\beta}\right)\right]\right.$$
$$\left. -J_{n-l}\left[k\left(1-e^{-i\tau\beta}\right)\right]+iJ_{n-l}\left[k\left(e^{-i\tau\beta}-1\right)\right]+iJ_{n-l}\left[k\left(1+e^{-i\tau\beta}\right)\right]\right)\Bigg|^2 \tag{2.22}$$

$$\left|\left\langle n\downarrow\left|\hat{U}_{kick}^2\right|\varphi_0\right\rangle\right|^2 \approx \frac{1}{4N^2}\Bigg|\sum_l (-1)^l e^{-i\tau\beta l}\left(iJ_{n-l}\left[-k\left(1+e^{-i\tau\beta}\right)\right]\right.$$
$$\left. +iJ_{n-l}\left[k\left(1-e^{-i\tau\beta}\right)\right]-J_{n-l}\left[k\left(e^{-i\tau\beta}-1\right)\right]+J_{n-l}\left[k\left(1+e^{-i\tau\beta}\right)\right]\right)\Bigg|^2 \tag{2.23}$$

The four summands in each matrix element are now the result of having mixed two times with eq. 1.23. Each mixing gives two summands (one being kicked to the left, the other one to the right) hence higher orders of $T$ will have a lot more terms to deal with. The quasimomentum $\beta$ influences the momentum distribution now: there is one additional multiplicator $e^{-i\tau\beta l}$ and the quasi-momentum is also contained in the kick strengths. In the limit $\beta \to 0$, kick strengths of $2k$, 0 and $-2k$ are obtained with the two contributions to 0 being separated by an $i$ and thus not interfering with each other once more. In this resonant case, eqs. 2.22 & 2.23 are no longer approximations but exact expressions.

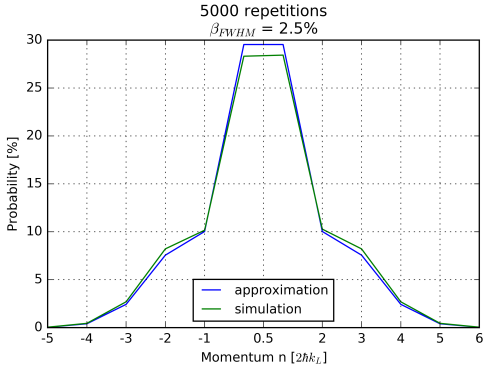


**Figure 2.4.:** Comparison of the approximation derived above with the walk simulation after two kicks. A good agreement is met except at the position of the initial momentum classes due to the approximation. Grid drawn for better illustration of the symmetry of the walk.

For $T = 1$ there are only two kick strengths of $\pm k$ whereas there are now the four above. A mathematical comparison to the Galton board will be given later on in section 2.5.

Averaging over five thousand of $\beta$-trajectories, a still good agreement with the simulation can be found in fig. 2.4. As already mentioned, the approximation is rather poor for momentum classes $n = 0$ and 1. This can be seen as a higher probability remaining at the initial momentum classes compared to the simulation. More about the simulation can be found in section 4.1.

### The general case for $T > 2$

Using the same approximation and addition $T$ repeated times, a similar structure for the matrix elements is found. The calculation in the appendix B is started using eq. 2.11 and leads to

$$\begin{aligned}\left\langle n\uparrow\middle|\hat{U}_{kick}^{T}\middle|\varphi_0\right\rangle \approx & \frac{i^n e^{-i\tau\beta n}}{\sqrt{2}^T N}\sum_l (-1)^l e^{-i\tau\beta(T-1)l} \\ & \times \sum_{m_1,\ldots,m_{T-2}} \left(\prod_{i=1}^{T-2} J_{m_i}\left[k\cdot e^{-i\tau\beta(T-i)}\right]\right) \\ & \times \sum_{m_{T-1}} J_{m_{T-1}}\left(k\cdot e^{-i\tau\beta}\right) J_{n-l-\sum_{i=1}^{T-2} m_i - m_{T-1}}(k)\ (*\uparrow)_T \Big|_{\sum m_i = n-l}\end{aligned} \tag{2.24}$$

The recurrence formulas found in eq. 2.13 have to be translated into a sum in the same fashion as done in eq. B.28. If done correctly, a $T$-time application of the addition rule gives back the similar structure as in eqs. 2.17 or 2.22 but now with $2^T$ Bessel summands.
Two preliminary calculations have to be carried out beforehand. The first one will show the consecution of further walk steps just by adding them to the argument of the Bessel function. For that assume $(*\uparrow)_T \equiv 1$. Then

$$\begin{aligned}& \sum_{m_1,\ldots,m_{T-2}} \left(\prod_{i=1}^{T-2} J_{m_i}\left[k\cdot e^{-i\tau\beta(T-i)}\right]\right) \\ & \times \underbrace{\sum_{m_{T-1}} J_{m_{T-1}}\left(k\cdot e^{-i\tau\beta}\right) J_{n-l-\sum_{i=1}^{T-2} m_i - m_{T-1}}(k)}_{=J_{n-l-\sum_{i=1}^{T-2} m_i}\left[k\left(1+e^{-i\tau\beta}\right)\right]}\end{aligned} \tag{2.25}$$

$$\begin{aligned}= & \sum_{m_1,\ldots,m_{T-3}} \left(\prod_{i=1}^{T-3} J_{m_i}\left[k\cdot e^{-i\tau\beta(T-i)}\right]\right) \\ & \times \underbrace{\sum_{m_{T-2}} J_{m_{T-2}}\left[k\left(1+e^{-i\tau\beta}\right)\right] J_{n-l-\sum_{i=1}^{T-3} m_i - m_{T-2}}\left(k\cdot e^{-i\tau 2\beta}\right)}_{=J_{n-l-\sum_{i=1}^{T-3} m_i}\left[k\left(1+e^{-i\tau\beta}+2e^{-i\tau\beta}\right)\right]}\end{aligned} \tag{2.26}$$

$$\stackrel{\text{iter.}}{=} J_{n-l}\left(k\sum_{j=0}^{T-1} e^{-i\tau j\beta}\right) \tag{2.27}$$

It is easy to include terms like $(-1)^{m_i}$ which then give the corresponding summands a negative sign instead of the positive one in eq. 2.27.
The second conclusion comes from the recurrence form in eq. B.10. A single mixing (including terms of $(-1)^m$ which come from the opposite kicking directions and omitting

the normalisation factor for now) is given by

$$\begin{pmatrix} (-1)^m & i \\ (-1)^m i & 1 \end{pmatrix} \tag{2.28}$$

The diagonal entries are the two ratchet currents if there was no mixing present. The opposite signs indicate the opposite directions of the currents. If a walker has already been shifted e.g. to the right, it will be further driven in this direction with each consecutive kick.
The off-diagonal entries now couple the two currents. If a walker was once again shifted to the right, the cross terms shift it to the left and add a phase $i$. Due to the balanced coin the same holds for the opposite directions. The final momentum distribution will then contain $2^T$ summands each being a Bessel function $J_{n-l}\left(k \cdot *\right)$ where $*$ is a linear combination of the elements $\left\{1, e^{-i\tau\beta}, \ldots, e^{-i\tau\beta(T-1)}\right\}$, i.e.

$$* = \sum_{j=0}^{T-1} a_j \left(e^{-i\tau\beta}\right)^j \qquad \text{with } a_j = \pm 1 \quad \forall j$$

The summands will be weighted with an additional prefactor $i^\alpha$ where $\alpha$ denotes the amount of turns during the whole walk. The final momentum distribution for an arbitrary walk number $T \geq 1$ can then be expressed as

$$\begin{aligned} \left|\left\langle n \uparrow \middle| \hat{U}_{kick}^T \middle| \varphi_0 \right\rangle\right|^2 \approx \frac{1}{2^T N^2} \Bigg| \sum_l (-1)^l e^{-i\tau\beta(T-1)l} \\ \times \sum_{c\in\{0,1\}^T} i^{\alpha(c)} J_{n-l}\left[k \sum_{j=0}^{T-1} (-1)^{c_j} \left(e^{-i\tau\beta}\right)^j\right] \Bigg|^2 \end{aligned} \tag{2.29}$$

$$\begin{aligned} \left|\left\langle n \downarrow \middle| \hat{U}_{kick}^T \middle| \varphi_0 \right\rangle\right|^2 \approx \frac{1}{2^T N^2} \Bigg| \sum_l (-1)^l e^{-i\tau\beta(T-1)l} \\ \times \sum_{c\in\{0,1\}^T} i^{\beta(c)} J_{n-l}\left[-k \sum_{j=0}^{T-1} (-1)^{c_j} \left(e^{-i\tau\beta}\right)^j\right] \Bigg|^2 \end{aligned} \tag{2.30}$$

where $c = (c_0, c_1, \ldots, c_{T-1})$ with $c_i \in \{0, 1\}$ $\forall i$ and $\alpha(c)$ & $\beta(c)$ are the mentioned number of turns during one walk. The only difference is the opposite sign in the kicking strength and different prefactors (since $\alpha(c) \neq \beta(c)$ in general) for the summands.

A look on the terms having the highest energy $E(T) = \sum P(n,T) \cdot \frac{n^2}{2}$ (which is equivalent to the terms contributing the most to the walk spread) yields eq. 2.27 (for kicking strengths $k$ and $-k$ respectively) since it corresponds to the walker going throughoutly

in one of the directions. Evaluating the argument ($\equiv W_T$) gives

$$W_T = kT \qquad \beta = 0 \tag{2.31}$$

$$W_T = \exp\left(-i\tau\beta\frac{T-1}{2}\right) \cdot \frac{\sin\left(\tau\beta\frac{T}{2}\right)}{\sin\left(\tau\frac{\beta}{2}\right)} \qquad \beta \neq 0 \tag{2.32}$$

which is quite similar to the findings for the AOKR in eqs. 1.17 & 1.18. The difference can be explained by the approximation made using eq. 2.21 which is also why there is now a complex part left in the argument. In the resonance the ballistic motion is however refound because eqs. 2.29 & 2.30 are exact expressions (since no approximation is applied).

## 2.5. An analogy between the experimental quantum walk and the walk via the shift operator

The experimentally implemented walk has some interesting parallels to the initially formulated one using the unitary shift operator in eq. 2.33. For a better comparison the matrix elements of the first two steps for both walks (in the resonance limit $\beta \to 0$) with an initial external momentum class $|l\rangle$ will be calculated below (once again omitting the prefactors and the phase $e^{i\tau\beta(T-1)l}$ here).
We have the unitary shift operator

$$\hat{T} = \sum_i \Big[ |\downarrow\rangle\langle\downarrow| \otimes |i\rangle\langle i-1| + |\uparrow\rangle\langle\uparrow| \otimes |i\rangle\langle i+1| \Big] \tag{2.33}$$

compared to the kicking matrix

$$\hat{K} = e^{-ik\cos\hat{\theta}} \otimes |\uparrow\rangle\langle\uparrow| + e^{-ik\cos\hat{\theta}} \otimes |\downarrow\rangle\langle\downarrow| \tag{2.34}$$

Both walks are initialised with the Hadamard coin and mixed during the walk with

$$\hat{C} = \frac{1}{\sqrt{2}}\begin{pmatrix} 1 & i \\ i & 1 \end{pmatrix} \tag{2.35}$$

The respective matrix elements with respect to their internal levels are

$$\begin{pmatrix} \langle n|l\rangle \\ \langle n|l\rangle \end{pmatrix} \qquad\qquad \begin{pmatrix} \langle n|l\rangle \\ \langle n|l\rangle \end{pmatrix}$$

$$\overset{\hat{C}\circ\hat{T}}{\mapsto} \begin{pmatrix} \langle n|l+1\rangle + i\langle n|l-1\rangle \\ i\langle n|l+1\rangle + \langle n|l-1\rangle \end{pmatrix} \qquad \overset{\hat{C}\circ\hat{K}}{\mapsto} \begin{pmatrix} J_{n-l}(-k) + iJ_{n-l}(k) \\ iJ_{n-l}(-k) + J_{n-l}(k) \end{pmatrix}$$

$$\overset{\hat{C}\circ\hat{T}}{\mapsto} \begin{pmatrix} \langle n|l+2\rangle + (i-1)\langle n|l\rangle + i\langle n|l-2\rangle \\ i\langle n|l+2\rangle + (i-1)\langle n|l\rangle + \langle n|l-2\rangle \end{pmatrix} \quad \overset{\hat{C}\circ\hat{K}}{\mapsto} \begin{pmatrix} J_{n-l}(-2k) + (i-1)J_{n-l}(0) + iJ_{n-l}(2k) \\ iJ_{n-l}(-2k) + (i-1)J_{n-l}(0) + J_{n-l}(2k) \end{pmatrix}$$

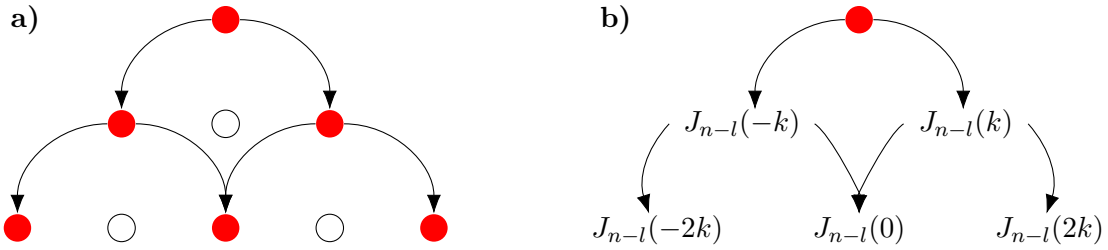


**Figure 2.5.:** Sketch of the analogy between the Galton board in a) in the quantum mechanical interpretation for the walk and the arguments of the single summands in the momentum distribution for the implemented walk in b).

The momentum shift $l \mapsto l \pm 1$ maps to applying a single kick with strength $\mp k$. Due to the plethora of couplings in the experimental implementation the momentum distribution on the right is not as coarse grained as the one on the left. However, the general structure of both walks is very similar. Fig. 2.5 underlines the similarity. In a) a Galton board is sketched where the walk starts at one grid position. The superposition in the walk directions leads to a departing of the walker in both directions for the first step. This procedure repeats itself at each populated grid position for every walk step. In the implemented quantum walk the system is equivalent to the superposition of single ratchets that differ in the effective kicking strength from each other. In the first step, only kicking strengths of $\pm k$ are obtained (whereas on the Galton board two opposite grid positions are reached). The next step yields four ratchets with strengths $-2k$, 0 and $2k$ with two ratchets having the same effect kicking strength in the resonant limit. The Galton board also has the three grid positions $l-2$, $l$ and $l+2$ populated.
The populated grid positions on the Galton board can therefore be related to the effektive kicking strengths (in multiples of $k$) of the implemented quantum walk.

## 2.6. Summary

The reformulation of the kicking operator into momentum space revealed a structure of summands in the final momentum distributions similar to the Galton board (quincunx). There is no direct match, as on the Galton board one shifts to the very adjacent momentum classes, whereas in the quantum walk the similar structure is contained in the effective kick strengths of each summand. Thus, a shift from momentum class 0 to $\pm 2$ on the Galton board corresponds to an effective kick strength of $\mp 2k$. We note, however, that the respective summand still couples all other momentum classes (but with decreasing weight). A scheme of the comparison is shown in fig. 2.5. This structure will also be obtained for higher kick counts $T$ but will grow exponentially in the number of summands for the momentum distribution. In the shown limit $\beta \to 0$ the complexity can be reduced with the help of the symmetry property of the Bessel functions. This

way, the effective growth in summands goes linearly since only a maximal kick strength of $kT$ can be reached by $T$ kicks, giving $T$ summands.[2].
In the non-ideal case a similar method might be applicable by further examination of the properties of eqs. 2.29 & 2.30. These two formulas contain the main result of above calculations.

The resulting momentum distributions are given in chapter 4 where they are compared to walk simulations using a quantum map. For the resonance limit $\beta \to 0$ a comparison is also drawn with the analytical theory for the ideal walk case which is reviewed in the following chapter, based on [17].

[2]Because the relative sign of the momentum class can be ignored due to the symmetry property.

# 3. Recap of the analytic theory for the ideal walk

An analytic expression for the resonant walk, i.e. $\beta = 0$, was already given by Caspar Groiseau in [17]. The main train of thought is summarized briefly and then compared to the theory developed in section 2.2.

## Finding the recursion

The kicking matrix in eq. 1.29

$$\begin{aligned} \hat{U}_{kick} &= \frac{1}{\sqrt{2}} \begin{pmatrix} e^{-ik\cos\hat{\theta}} & ie^{ik\cos\hat{\theta}} \\ ie^{-ik\cos\hat{\theta}} & e^{ik\cos\hat{\theta}} \end{pmatrix} \\ &=: \frac{1}{\sqrt{2}} \begin{pmatrix} a_{11} & a_{12} \\ a_{21} & a_{22} \end{pmatrix} \end{aligned} \tag{3.1}$$

contains a general property, that is the relations between the cross-paired elements. They are related by

$$a_{11}^* = a_{22} \tag{3.2}$$

$$a_{12}^* = -a_{21} \tag{3.3}$$

which stems from the property of each kick matrix $\hat{K}$ and mixing $\hat{M}$ (eqs. 1.28 & 1.25) having this property already. A multiplication conserves the characteristics.
With the short hand notations

$$E := e^{ik\cos\hat{\theta}} \tag{3.4}$$

$$E^* := e^{-ik\cos\hat{\theta}} \tag{3.5}$$

$$z := E^* + E \tag{3.6}$$

$$\tilde{z} := E^* - E \tag{3.7}$$

and omitting the $\sqrt{2}$-prefactor the first few step operators are

$$\hat{U}^1 = \begin{pmatrix} E^* & iE \\ iE^* & E \end{pmatrix} \tag{3.8}$$

$$\hat{U}^2 = \begin{pmatrix} E^*\tilde{z} & iEz \\ iE^*z & E\tilde{z} \end{pmatrix} \tag{3.9}$$

$$\hat{U}^3 = \begin{pmatrix} E^*\left(\tilde{z}z - 2\right) & iE\left(z^2 - 2\right) \\ iE^*\left(z^2 - 2\right) & -E\left(\tilde{z}z + 2\right) \end{pmatrix} \tag{3.10}$$

$$\hat{U}^4 = \begin{pmatrix} E^*\left(z^2\tilde{z} - 2z - 2\tilde{z}\right) & iE\left(z^3 - 4z\right) \\ -iE^*(\dots)^* & E(\dots)^* \end{pmatrix} \tag{3.11}$$

$$\dots \tag{3.12}$$

$$\hat{U}^{T+1} = \begin{pmatrix} E^*p_1^T & iEp_2^T \\ \dots & \dots \end{pmatrix} \tag{3.13}$$

The outer structure in form of the original mixing matrix is conserved and only altered by polynomials of $z$ and $\tilde{z}$. They differ slightly for the two relevant entries and will be denoted $p_{1,T}$ and $p_{2,T}$ respectively or $p_{1/2,T}$, if both are addressed. From the above matrix elements it can be proven via induction that the recursion

$$p_{1/2,T} = z \cdot p_{1/2,T-1} - 2 \cdot p_{1/2,T-2} \tag{3.14}$$

relates the kick step to its precessors.

## Solving the recursion relation

The recurrence relation in eq. 3.14 was already solved in [17] where two non-trivial solutions could be found. We will now add a short proof that the found solutions are the only solution of eq. 3.14.

The ansatz here is to assume $p_{1/2,T} \equiv \left(p_{1/2}\right)^T$, i.e. $\exists\, x \in \mathbb{C} \setminus \{0\} : p_{1/2,T} = x^T$.
Be $\mathcal{L}$ the set of all solutions[1] of eq. 3.14 which is assumed to be finite for now, that means $\mathcal{L} = \{x_1, x_2, \cdots, x_l\}$.
A general solution is of the form

$$p_{1/2,N} = \sum_{i=1}^{l} c_i x_i^N, N \in \mathbb{N}$$

[1] Trivially, 0 is also a solution of the recursion. It is, however, the one indicating the absence of a kick and not of interest here

$$
\begin{aligned}
\Rightarrow p_{1/2,N+1} =& \sum c_i x_i^{N+1} = \sum \underline{(x_i)} \cdot c_i x_i^N \\
=& z\left(\sum c_i x_i^N\right) - 2\left(\sum c_i x_i^{N-1}\right) = \sum (z) c_i x_i^N - \sum \left(\frac{2}{x_i}\right) c_i x_i^N \\
=& \sum \underline{\left(z - \frac{2}{x_i}\right)} c_i x_i^N \\
& \Leftrightarrow x_i = z - \frac{2}{x_i} \quad \forall\ i \in \{1, \cdots, l\} \\
& \Leftrightarrow x_i^2 = z x_i - 2 \quad \forall\ i \in \{1, \cdots, l\}
\end{aligned}
$$

where in the last two steps the underlined terms were compared to each other. The problem is thus reduced to a quadratic formula ($l \equiv 2$) with the only two possible solutions

$$x_{1/2} = \frac{z \pm \sqrt{z^2 - 8}}{2} \tag{3.15}$$

$$p_{1/2,T} = c_1 x_1^T + c_2 x_2^T \tag{3.16}$$

where the constants $c_i$ can be found looking at the first two matrix polynomials in eqs. 3.8 & 3.9 which gives

$$p_1^T = \frac{1}{2}\left(1 + \frac{2\tilde{z} - z}{\sqrt{z^2 - 8}}\right)\left(\frac{z + \sqrt{z^2 - 8}}{2}\right)^T + \frac{1}{2}\left(1 - \frac{2\tilde{z} - z}{\sqrt{z^2 - 8}}\right)\left(\frac{z - \sqrt{z^2 - 8}}{2}\right)^T \tag{3.17}$$

$$p_2^T = \frac{1}{2}\left(1 + \frac{z}{\sqrt{z^2 - 8}}\right)\left(\frac{z + \sqrt{z^2 - 8}}{2}\right)^T + \frac{1}{2}\left(1 - \frac{z}{\sqrt{z^2 - 8}}\right)\left(\frac{z - \sqrt{z^2 - 8}}{2}\right)^T \tag{3.18}$$

## Rewriting the general solution

The quite tedious solutions are now cast into polynomials with $E$ and/or $E^*$ as their arguments. $\forall N \in 2\mathbb{N}$ the calculations of the two relevant matrix elements in eq. 3.1 yield

$$a_{11,N} = \sum_{l=0}^{N} a_{l,1} e^{ik\cos\hat{\theta}(N-2l-1)} \tag{3.19}$$

$$a_{22,N} = i\sum_{l=0}^{N} a_{l,2} e^{ik\cos\hat{\theta}(N-2t+1)} \tag{3.20}$$

and their respective prefactors

$$\begin{aligned} a_{l,1} =& \frac{1}{2^N} \sum_{j=0}^{\frac{N}{2}} \left[ \binom{N}{2j} - \binom{N}{2j+1} \right] \sum_{m=0}^{l} \binom{j}{m} \binom{N-2m}{l-m} (-8)^m \\ & - \frac{2}{2^N} \sum_{j=0}^{\frac{N}{2}} \binom{N}{2j+1} \sum_{m=0}^{l} \binom{j}{m} \binom{N-2m-1}{l-m} (-8)^m \\ & + \frac{2}{2^N} \sum_{j=0}^{\frac{N}{2}} \binom{N}{2j+1} \sum_{m=0}^{l-1} \binom{j}{m} \binom{N-2m-1}{l-m-1} (-8)^m \end{aligned} \tag{3.21}$$

$$a_{l,2} = \frac{1}{2^N} \sum_{j=0}^{\frac{N}{2}} \binom{N+1}{2j+1} \sum_{m=0}^{l} \binom{j}{m} \binom{N-2m}{l-m} (-8)^m \tag{3.22}$$

## Final momentum distribution

Carrying out the calculations leads to

$$P(n,N) = |\langle n \uparrow | \varphi(N) \rangle|^2 + |\langle n \downarrow | \varphi(N) \rangle|^2 \tag{3.23}$$

$$\begin{aligned} =& \frac{1}{2^{N+2}} \Bigg[ \left( \sum_{l=0}^{N} a_{l,1} \Big[ J_n[(N-2l-1)k] - J_{n-1}[(N-2l-1)k] \Big] \right)^2 \\ & + \left( \sum_{l=0}^{N} a_{l,2} \Big[ J_n[(N-2l+1)k] - J_{n-1}[(N-2l+1)k] \Big] \right)^2 \\ & + \left( \sum_{l=0}^{N} a_{l,1} \Big[ J_n[-(N-2l-1)k] - J_{n-1}[-(N-2l-1)k] \Big] \right)^2 \\ & + \left( \sum_{l=0}^{N} a_{l,2} \Big[ J_n[-(N-2l+1)k] - J_{n-1}[-(N-2l+1)k] \Big] \right)^2 \Bigg] \end{aligned} \tag{3.24}$$

which was shown to be extendable to more initial momentum classes [17].

This result also contains the Bessel functions of the first kind, $J_m$ but the discovered structure of $2^T$ Bessel summands in eqs. 2.29 & 2.30 is here encoded in the prefactors for summands with the same effective kicking strength (note the $l$-dependency of the prefactors of the Bessel functions in eq. 3.24). A similar recurrence property was found individually in eqs. 2.13 & 3.14 which originates from the mixing with eq. 1.25 in both cases.

# 4. Simulation results for the experimental findings

In this chapter we will have a closer look on comparing the developed theory in chapter 2 with the ideal case in chapter 3 in quantum resonance as well as with a numerical study using a so called quantum map which is explained in section 4.1.
The second part will focus on the experimental results of the experiment explained in section 1.3 which was carried out at Oklahoma State University. All experimental data in the chapters 4.2.2 & 5.1.2 are with courtesy of Gil Summy and Siamak Dadrasmarani and are unpublished until this writing [37].
They are the main motivation for the developed theory as it addresses one of the core walk limitations, namely the dephasing due to near-resonant quasimomenta. Another measurable effect is the thermal cloud around the BEC which will be considered (among some further explanaition regarding the simulation) in the next section.

## 4.1. Numerical Implementation

### Quantum map

As inter-particle interactions in the BEC become neglegible with the low temperature, the walk can be treated as a single-particle-theory. For its simulations, the available momentum classes have to be of finite size $N$. It is best advised to choose a set size with a power of 2 as fast Fourier transformations become most efficient[1]. In position space this finite size yields a discretisation and creates a grid of

$$\theta_i = \frac{2\pi}{N} i \tag{4.1}$$

and momentum classes of

$$n = -N/2, -N/2 + 1, \ldots, N/2 - 1 \tag{4.2}$$

Because of the two internal levels we accredit each of them their own wavefunction (but normalized to 0.5 to give a normalized total wavefunction) where there is a complex data entry for each momentum class allocated. An initalisation in momentum space follows

[1] Modern numerical implementations of the FFT also work with odd array lengths and even but worst with prime array lengths.

eq. 1.27 and is of the form

$$\begin{aligned}\psi_\uparrow(n=0) &= \frac{1}{2}\\ \psi_\downarrow(n=0) &= \frac{1}{2}\\ \psi_\uparrow(n=1) &= -i\cdot\frac{1}{2}\\ \psi_\downarrow(n=1) &= -i\cdot\frac{1}{2}\end{aligned} \tag{4.3}$$

As desribed already, the two parts of the Floquet operator are well applicable in position or momentum space respectively. This demands the use of the (inverse) fast Fourier transformation in order to switch from one space to the other.
A single kick step is the inverse transformation into position space and the application of the kick

$$e^{\pm ik\cos\theta_i} \tag{4.4}$$

on each grid point. Due to the complex data type, this can be multiplied straightforward. The only caveat here is that one wavefunction is throughoutly kicked with strength $k$ whereas the other with $-k$.
After the fast Fourier transformation back into momentum space the reordering by the FFT-routine has to be inversed by applying an IFFT-shift. The free evolution

$$e^{-\frac{i}{2}\tau {p_i}^2} \tag{4.5}$$

is applied which includes the quasi-momentum $p = n + \beta$ as well. The last step is the mixing of the two internal levels with eq. 1.23.
The joint probability is then drawn from the sum of the two absolute squares of the complex values corresponding to the same momentum class. Since the initialisation was chosen to create a totally normalized wavefunction, no further normalisation is needed. An example for the numerical implementation is given in appendix C.

When dealing with a finite width in quasi-momentum a Monte-Carlo fashioned average is used

$$\bar{P} = \frac{1}{N}\sum_{i=1}^{N} P_i \tag{4.6}$$

This average assumes that each particle in the BEC contributes a single quasimomentum in contrast to the coherent superpostion in eq. 1.9. A justification was already given in section 1.1.1. Typical samples sizes are between 5000 and 10000 particles each with an individual $\beta$-value. As mentioned in section 1.3, the number of BEC atoms is in the same order of magnitude.

### Thermal cloud effects

In the experimental set-up the creation of the BEC does include a thermal cloud which is affected by the microwave pulses to some extent. For the given experimental implementation the momentum distribution of the thermal cloud can be well assumed to be Gaussian around momentum class $0$[2] with a width of half a Brillouin zone. At this level the distribution for the quasi-momentum follows the same shape [23]. Since these values are far from resonance in general the behaviour of the cloud is mostly static around the initial Gaussian profile and thus does not change much during the kicking sequence. This results in a higher momentum probability around the initial momentum classes as the simulations would show without this effect. The experimental data however, show such a behaviour, confirming a thermal cloud effect with a ratio of $10 - 15\%$ compared to the BEC as seen below in the comparison.

### Taking into account the experimental imaging process

The momentum distribution for each kick step is experimentally detected using the time-of-flight screening method. In the common representation, the distribution has a profile perpendicular to the walk axis due to the effects of gravity. This profile is then stacked in the time window between two consecutive kicks just before the actual screening point. This may give an impression of a long measurement process but it is only done for better representation. We also remark a larger Gaussian FWHM in the experimental momentum distributions than actually present for the experiment. This might be due to the time-of-flight method as well as the thermal cloud part being distributed uniformly over the whole momentum class.
In the simulations we consider the imaging process by giving each momentum class two Gaussian profiles.Their respective parameters are taken from fits of the actual experimental image data. It allows for a more visible comparability between the two data sets.

## 4.2. Comparison of simulation, developed theory and experiment

### 4.2.1. Comparison of the developed theory with the simulation

Figs. 4.1 and 4.2 show the comparison between the theory developed in chapter 2 and the simulation using the quantum map. Since for the ideal case the theory is an exact analytical expression, no deviation from the simulation is seen. The agreement is still fair for a low number of kicks at the current experimental width in quasimomentum of about 2.5%, see fig. 4.2c, or for a lower width like 0.5% depicted in fig. 4.2a & b. Since the effective quasimomentum in eq. 2.24 grows with $\beta T$ linearly in time the approximation done in eq. 2.21 can no longer be justified, hence a higher deviation from

[2]The thermal cloud is not altered by the initial Bragg pulse explained in eq. 1.26

the simulation in fig. 4.2d. The approximation is the worst for the Bessel index $|n| \leq 2$ which is why there is a higher probability being in the centre compared to the simulation.

We also note the fact that due to the approximation made the resulting momentum distribution becomes symmetric in numerical simulations when run for a single $\beta$-trajectory. This is not the case in general. Instead the mean of two trajectories, one with $\beta_0$ and the other with $\beta_1 = -\beta_0$, can be considered. The average is now symmetric again for all $\beta_0$ yielding a better agreement with the developed theory.
A minor problem is the exponential growth of summands in the momentum distribution. A test of the running time in the resonance limit is shown in fig. 4.3. In this figure the algorithms implementing the introduced theory of chapter 2 is compared with the theory of the resonant case presented in chapter 3 and the simulation using the quantum map described in section 4.1. The two latter only grow somewhat polynomially with the walk length but for the developed theory an exponential running time is found. This is however due to the fact that no optimisation for the eqs. 2.29 & 2.30 was applied. As mentioned in section 2.6 the maximal kicking strength in the Bessel summands grows only linearly with the walk steps. A further treatment of the $2^T$ components should reduce them to only $2T$ remaining ones having pairwisely different kicking strengths. This is implicitly implemented in the ideal case hence the speed-up here.

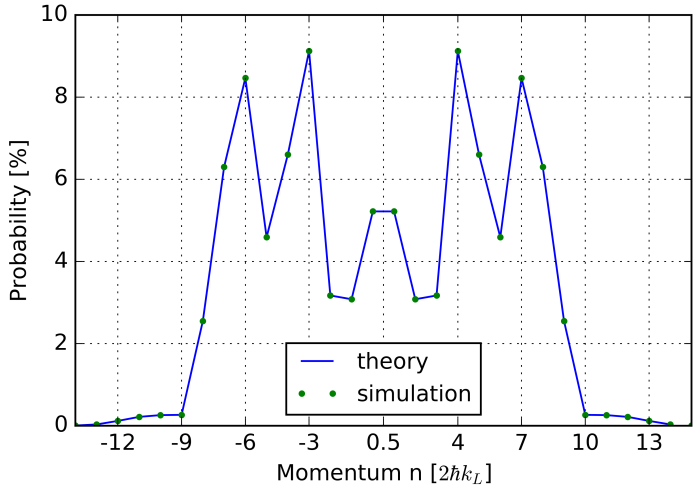


**Figure 4.1.:** Comparison of simulation and theory for the ideal case $\beta \to 0$. Since the theory in the resonance case is no longer an approximation, no deviations between the two approaches are expected and seen above. Grid drawn to underline the symmetry of the walk.

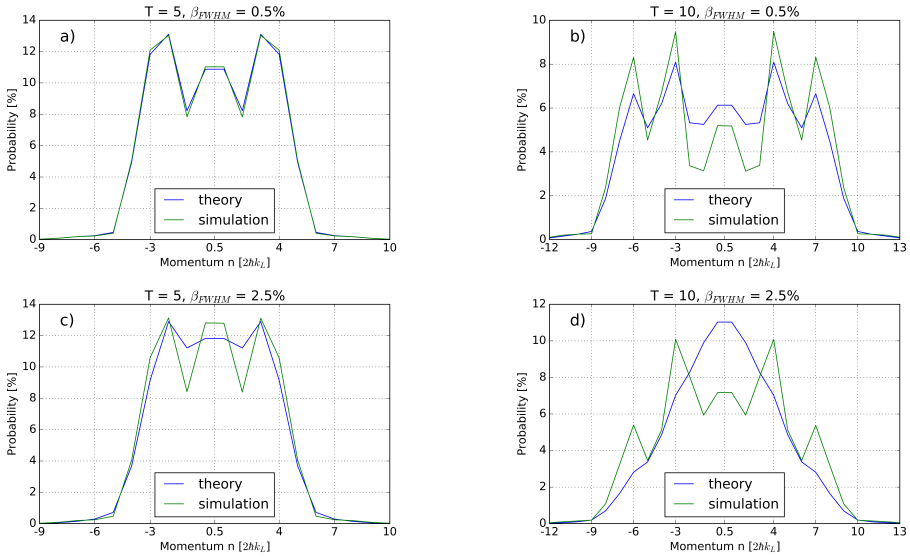


**Figure 4.2.:** Comparison of the simulation with the approximative theory for $\beta_{FWHM} = 0.5, 2.5\%$ for short and intermediate kick numbers. a) and c) with $T = 5$, b) and d) for $T = 10$ with less good agreement. Same holds for increasing the width from 0.5% in a) and b) to 2.5% for c) and d). Grids drawn to underline the symmetry of the walk.

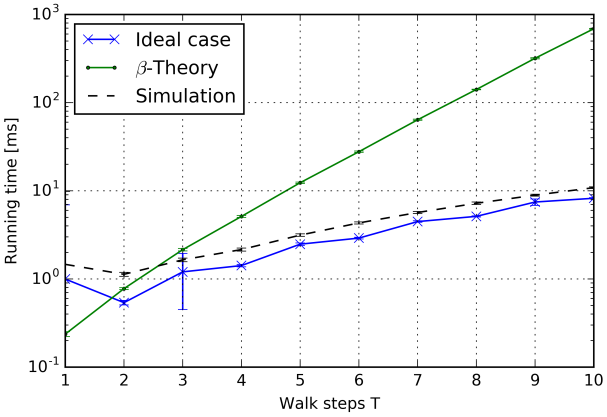


**Figure 4.3.:** Running time for the algorithm calculating the ideal walk distribution over the intervall $[-T, T]$ for different walk steps $T$. The grid length $N$ for the simulation is always minimized such that $N \geq 2T$ is always fulfilled. The simulation (black) and the theory represented in chapter 3 (blue) require way less computational time than summing up the summands in eqs. 2.29 & 2.30 which is depicted by the highest (green) line. The error bars correspond to one standard deviation of 100 runs of the same algorithm.

### 4.2.2. Comparison with the experiment

In order to compare the experiment with the simulations for all time steps and momentum classes, false-color plots illustrate the quality of the matching (figs. 4.4 - 4.6). The x-axis is the time axis corresponding to the walk steps taken. The y-axis shows the different momentum classes and the population distribution is encoded in a heat map. A dark blue color corresponds to a probability of 0 scaling up to red for a probability of 0.5.
The walk starts in the initialized momentum classes of eq. 1.27 und spreads ballisticly outwards over time as more momentum classes are getting coupled with each other. Quite distinctive for all images is the Gaussian peak, especially for higher kick counts. It corresponds to the thermal cloud reviewed in section 4.1 as well as the dephasing due to the near-resonant quasi-momenta discussed in chapter 2.

For the simulations accompanying the experimental data, the parameters to adjust are the kicking strength $k$, the width of the near-resonant quasimomentum distribution $\beta_{FWHM}$ and the degree of influence from the thermal cloud (as a fraction of the BEC). As mentioned before the spontaneous emission was not included in the simulations as its effect on the walk was barely noticable. Adjustment is required as the experiment gives values for $k$ and $\beta_{FWHM}$ but with some uncertainty thus the simulation parameters have to be found within the error windows of the experimental ones. In fig. 4.4 for example, the experiment was run for $k = 1.4$ but the simulation suggests an effective kick strength of 1.45 to 1.5 with a width of approx. 2.5%.
Consecutively, the thermal cloud fraction was steadily increased until the centered peak

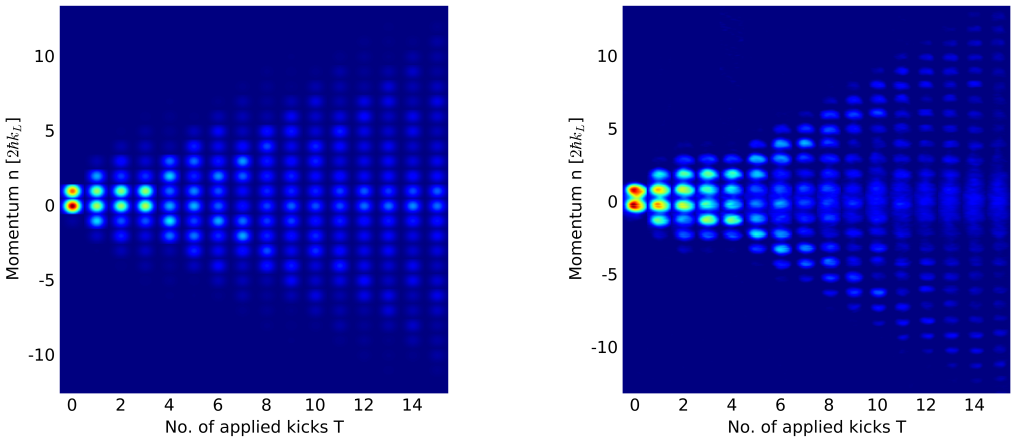


**(a)** Simulation **(b)** Experiment

**Figure 4.4.:** Comparison of the experiment with the best fit in the simulation for $k \approx 1.5$. Experimental data from [37].

for low kick steps (which would otherwise not be seen in the simulations) matches the experimental data. This is the case for a fraction of around 15%. The overall agreement is fairly good as the outgoing peaks as well the remaining one in the centre match quite well.

## Biased walks

So far, all investigated walks were symmetric around the initial momentum classes $n = 0, 1$ by the choice of the coins (eqs. 1.22 and 1.23 were both balanced) and the detuning chosen to be halfway between the hyperfine levels (see fig. 1.4) which gave the same absolute kicking strength for both levels. Either of these conditions altered would steer the walk in one preferred direction resulting in a biased walk like given in fig. 4.5.

In the upper two plots both coins were given a bias $\rho$ e.g. as for the walk coin

$$\hat{C}_{bias} = \begin{pmatrix} \sqrt{\rho} & i \cdot \sqrt{1-\rho} \\ i \cdot \sqrt{1-\rho} & \sqrt{\rho} \end{pmatrix} \tag{4.7}$$

(and in the same fashion for the Hadamard gate) meaning that one level was constantly assigned a higher population than the other. This inequality due to the different kick directions of the levels results in a directed walk.

The same can be achieved by altering the detuning instead of biasing the coins. In this case the detuning will be closer to one of the internal levels which means a weaker kick for the corresponding walk direction and a stronger one in the other. This also results in a directed motion as seen in fig. 4.5c & d where $k_\uparrow = 1.7$ and $k_\downarrow = 1.0$.

The walk is therefore easily steerable in the experiment which might make it interesting

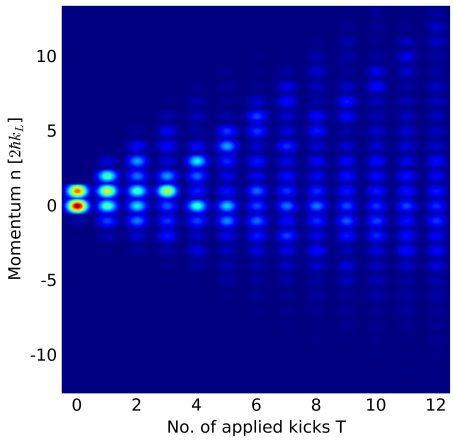


**(a)** Biased coin, simulation

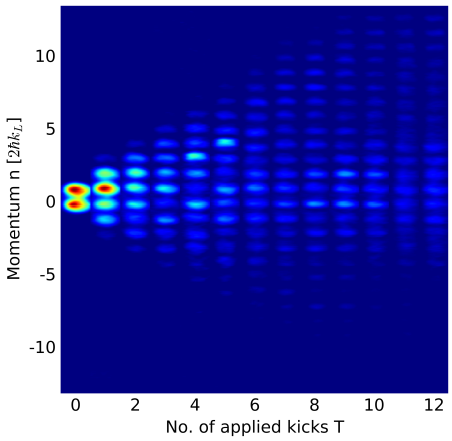


**(b)** Biased coin, experiment

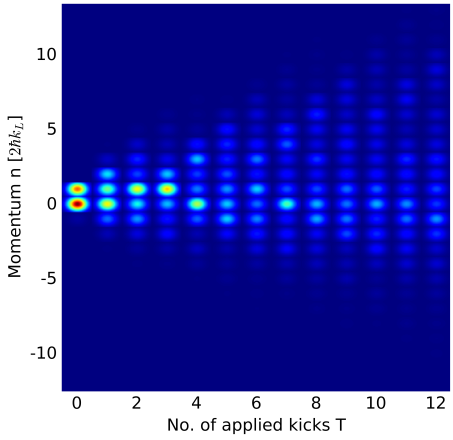


**(c)** Biased kicking strengths, simulation

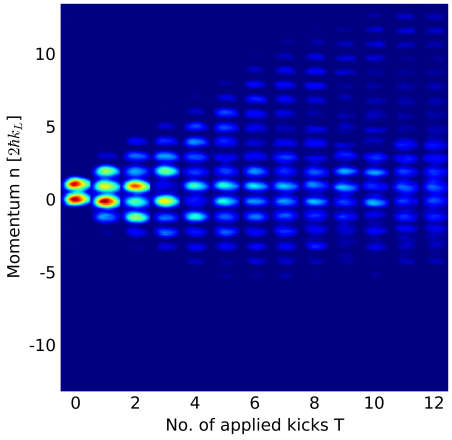


**(d)** Biased kicking strengths, experiment

**Figure 4.5.:** Comparison of the biased walks in the experiment with the simulations. $\rho = 0.7$ chosen for the biased coins and $k = 1.5$ as in fig. 4.4. Experimental data from [37].

for quantum computational (search) algorithms.

### Transition to classical behaviour by randomizing the mixing phase

The transition from quantum to classical behaviour is an interesting topic on its own already. The implemented walk also has such a transition which is however not due to decoherence as the effects of SE was negligible in the experiment. The transition is still achieved by randomizing the offset for the phase $\chi$ in eq. 1.25 uniformly over an intervall $[-\alpha \cdot 2\pi, \alpha \cdot 2\pi]$. This is equivalent to introduce noise to the system, in this case for the phase of the microwave. The behaviour of the walk now depends on the offset phase $\alpha$

which can be interpreted as a measure of the quantumness. The result is seen in fig. 4.6. Already at $\alpha = 4\%$ the walk centres more compared to fig. 4.4b which has the same parameters but a fixed phase. With a totally random phase (corresponding to $\alpha = 1/2$) classical behaviour is expected which the walk shows by approaching a Gaussian shape even for the first few walk steps.

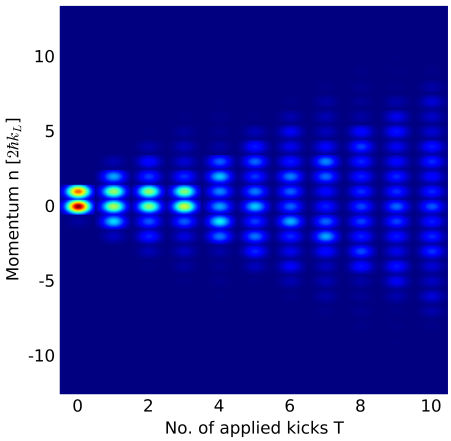


**(a)** Coin randomness 4%, simulation

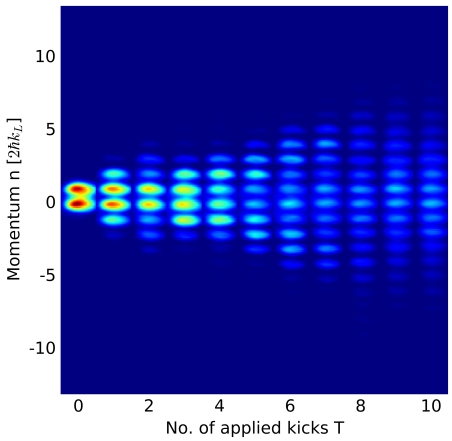


**(b)** Coin randomness 4%, experiment

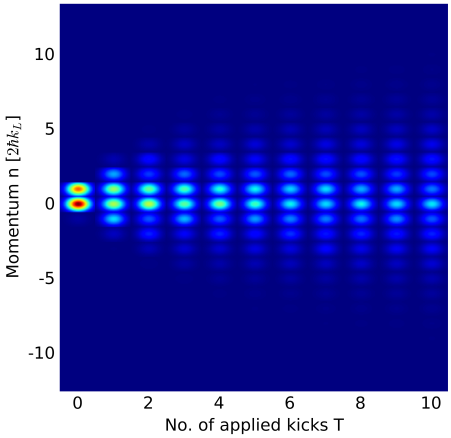


**(c)** Coin randomness 100%, simulation

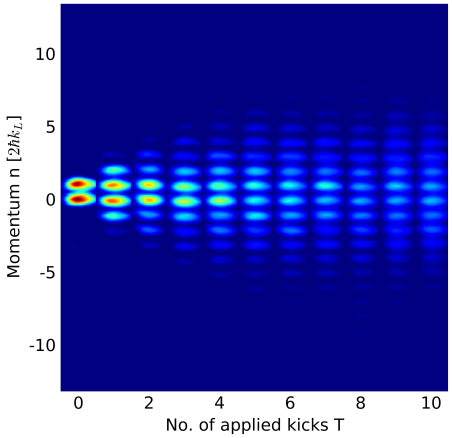


**(d)** Coin randomness 100%, experiment

**Figure 4.6.:** Comparison of the walks, where the offset of the mixing phase is uniformly distributed within $\pm\alpha \cdot 2\pi$, in the experiment with the simulations. Experimental data from [37].

## 4.3. Summary

The approximation - as discussed already around eq. 2.21 - is justified for small deviations of the quasi-momentum from the resonant case $\beta_{res} = 0$. Since the effective quasi-momentum grows linearly over time (see the $\beta T$ terms in eqs. 2.29 & 2.30), the approximation is only valid for a small number of walk steps taken. The same holds for a small FWHM in the corresponding $\beta$-distribution considered for the classical average in eq. 4.6. However, the theory developed in chapter 2 gives a more intuitive explanation for the resonant case than the theory reviewed in chapter 3.

The simulations for the comparison with the experimental findings in [37] furthermore take into account the impact of the thermal cloud surrounding the Bose-Einstein condensate, according to section 4.1. An overall good agreement is found. Moreover, the simulation parameters were within the uncertainty windows of the experimentally measured ones. This justifies the theoretical approach of the atom optics kicked rotor combined with quantum ratchets.

# 5. Walk reversal

In the last chapter in section 4.2.2, the controllability of the walk was demonstrated by steering it into one of two possible directions. Another controll feature is the reversal of single or multiple walk steps. Since the walk evolves coherently and unitarily, it is possible to reverse all taken steps in a walk. If the kicking matrix

$$U_{kick} = \frac{1}{\sqrt{2}} \begin{pmatrix} 1 & i \\ i & 1 \end{pmatrix} \begin{pmatrix} e^{-ik\cos(\hat{\theta})} & 0 \\ 0 & e^{ik\cos(\hat{\theta})} \end{pmatrix} \equiv \hat{M}\left(\frac{\pi}{2}, -\frac{\pi}{2}\right) \cdot \hat{K} \tag{5.1}$$

is applied $T$ times, application of its Hermitian conjugate for $T$ times should revert the momentum probability to its origin:

$$U_{kick}^{-1} = \frac{1}{\sqrt{2}} \begin{pmatrix} e^{ik\cos\hat{\theta}} & 0 \\ 0 & e^{-ik\cos\hat{\theta}} \end{pmatrix} \begin{pmatrix} 1 & -i \\ -i & 1 \end{pmatrix} \equiv \hat{K}^{-1} \cdot \hat{M}\left(\frac{\pi}{2}, \frac{\pi}{2}\right) \tag{5.2}$$

The kick operator $\hat{K}$ can be inversed by applying two Pauli-like (rotation) matrices. This leads to

$$U_{kick}^{-1} = \hat{M}\left(\pi, \pm\frac{\pi}{2}\right) \cdot \hat{K} \cdot \hat{M}\left(\pi, \mp\frac{\pi}{2}\right) \cdot \hat{M}\left(\frac{\pi}{2}, \frac{\pi}{2}\right) \tag{5.3}$$

for the inverse kicking matrix. Here, $\hat{M}$ denotes the mixing coin from eq. 1.25.
Experimentally, the application of three microwave pulses per step is quite challenging. An easier way to implement a reversal is to switch to ratchet currents, i.e. not applying the mixing $\hat{M}$ at all, and to reverse the populations after $T$ kicks. Another $T$ ratchet steps let the ballistic peaks move inwards again. The absence of the mixing between to consecutive kicks means working indifferently from the internal levels.

A protocoll of such a procedure would be for $T \in 2\mathbb{N}$:

1. Initialisation with the Hadamard coin $\hat{C}_{Had}$ (eq. 1.22)
2. $T/2$-time application of $\hat{K}$ (eq. 1.28)
3. Application of a $\pi$-pulse, i.e. $\hat{M}(\pi, 0)$, for a population swap
4. Another $T/2$-time application of $\hat{K}$
5. Reset of step one but with an arbitrary phase $\chi$, i.e. applying $\hat{M}(\pi/2, \chi)$

In the ideal case of no width in quasi-momentum this gives

$$\hat{U}_{total} = \hat{C}^{\dagger}_{Had}(\chi)\hat{K}^{T/2}\hat{M}(\pi,0)\hat{K}^{T/2}\hat{C}_{Had} \tag{5.4}$$

$$= \hat{C}^{\dagger}_{Had}(\chi)\begin{pmatrix} 0 & 1 \\ -1 & 0 \end{pmatrix}\hat{\mathbb{1}}_n\hat{C}_{Had} \tag{5.5}$$

$$= \frac{1}{2}\begin{pmatrix} -e^{-i\chi}-1 & -e^{-i\chi}+1 \\ e^{i\chi}-1 & -e^{i\chi}-1 \end{pmatrix}\hat{\mathbb{1}}_n \tag{5.6}$$

where $\hat{\mathbb{1}}_n$ is the identity operator acting in momentum space.
Applied on the initial state $|\varphi_0\rangle \otimes |\downarrow\rangle$ this gives a final state of

$$|\varphi_0\rangle \otimes \left(ie^{-i\frac{\chi}{2}} \cdot \sin\left(\frac{\chi}{2}\right)|\uparrow\rangle - e^{i\frac{\chi}{2}} \cdot \cos\left(\frac{\chi}{2}\right)|\downarrow\rangle\right) \tag{5.7}$$

and thus the population of one internal level goes with $\sin^2(\frac{\chi}{2})$ for $|\uparrow\rangle$ and with $\cos^2(\frac{\chi}{2})$ for $|\downarrow\rangle$.

## 5.1. Results of the implementations

The reversal of the quantum walk in the same fashion as implemented in chapter 4 is shown to be impossible at the given width in quasimomentum in the next section. This is the reason for switching to ratchet currents as explained above. For this kind of reversal the simulation compares well with the experimental results in section 5.1.2.
The third section concludes with a theoretical step towards probable matter-wave interferometry.

### 5.1.1. Reversal of the quantum walk

The numerical simulation confirms such a reversal in fig. 5.1, however the success of the procedure heavily depends on the width in quasi-momentum as the dephasing is not compensated in the experiment, see fig. 5.1. The dephasing is an effect of the near-resonant quasi-momenta $\beta \neq \beta_{res} = 0$. Their respective free evolution between two successive kicks produces a relative phase and also alters the effective kicking strength as derived in chapter 2. Due to the dephasing of single $\beta$-trajectories (as discussed around eq. 1.9) fig. 5.1 implies that at the current experimental level a walk reversal could not be implementable! As seen from eqs. 2.29 & 2.30, the momentum distribution is the sum of more and more terms all depending on the quasimomentum. Since its resulting dephasing is not compensated, this only allows a walk reversal for very small widths in quasimomentum. Switching to ratchet currents in section 5.1.2 as explained above evades this problem as the momentum distribution only has two summands of the form of eq. 1.16, one for each internal level.

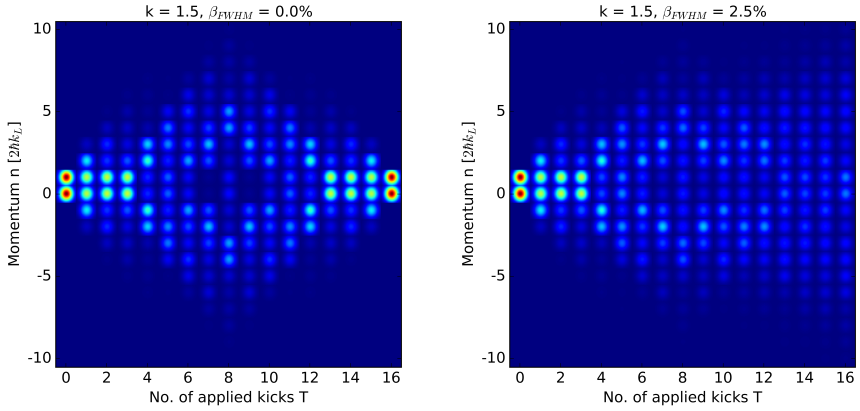


**(a)** Ideal reversal

**(b)** Experimentally accessible

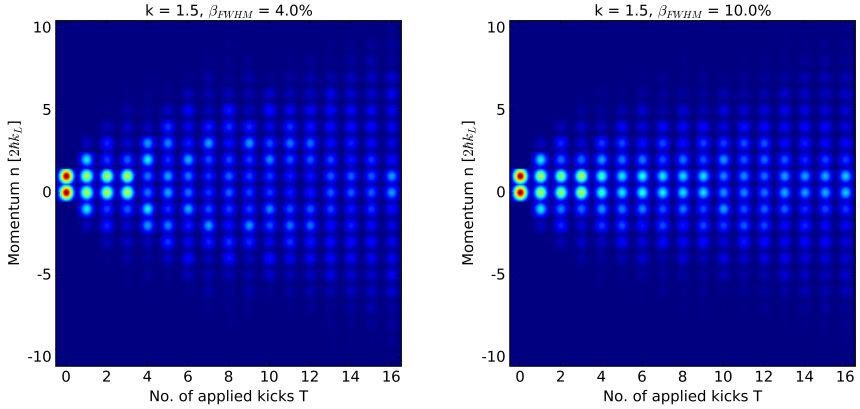


**(c)** Higher widths destroy any signs of reversal, here at 4% FWHM

**(d)** At this level even the normal walk is not observable anymore

**Figure 5.1.:** Simulated walk reversal of the quantum walk for different widths in quasi-momentum from the ideal case (a) to the off-resonance case (d).

### 5.1.2. Reversal of the ratchet current

This reversal is experimentally observable at the current setting and was tested for the two cases where the currents were reversed after $T = 3$ and $T = 5$ respectively. A high similarity between experiment and simulation is seen in fig. 5.2, both cases for $\beta_{FWHM} \approx 2.5\%$ and $k = 1.5$.

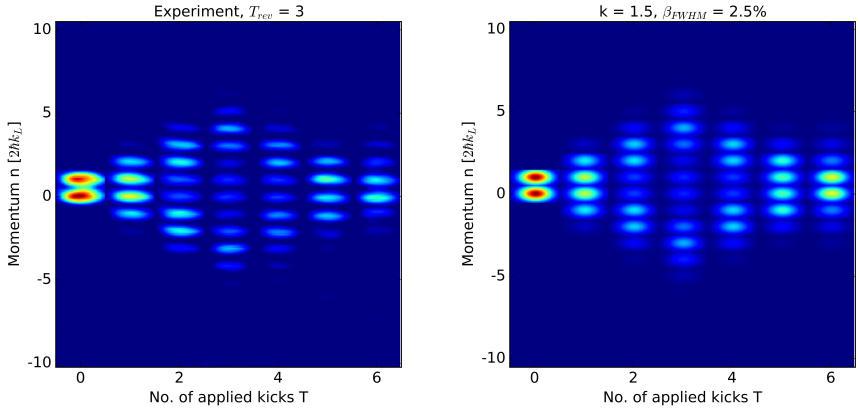


**(a)** Experiment for $T_{rev} = 3$ **(b)** Simulation for $T_{rev} = 3$

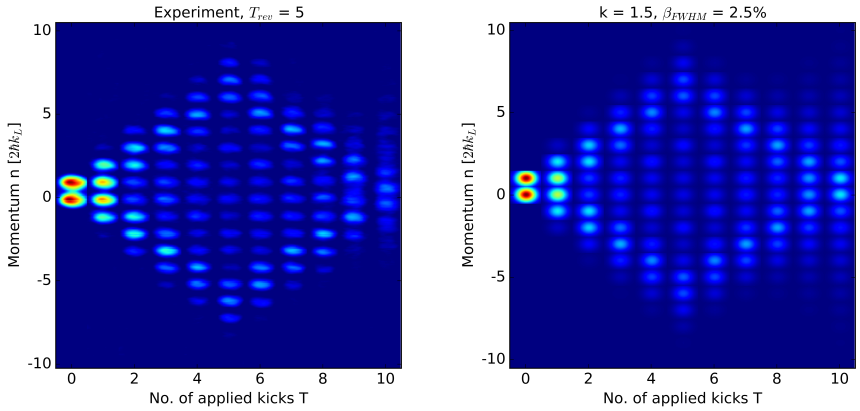


**(c)** Experiment for $T_{rev} = 5$ **(d)** Simulation for $T_{rev} = 5$

**Figure 5.2.:** Comparison of the reversal using a ratchet current. Good agreement is met for different reverse times $T_{rev}$ [42].

## 5.2. Towards interferometry

In this step a focus is placed at the population ratio of the two internal levels in depedence on the recombiner phase $\chi$. In quantum resonance, populations following $\sin^2(\frac{\chi}{2})$ and $\cos^2(\frac{\chi}{2})$ are expected. This is still the case for a finite width in quasi-momentum but with an amplitude $A = A(\beta_{FWHM}, T)$ mixing the two levels more with each other. This effect also increases with the number of kicks $T_{rev}$ up to the population swap because the dephasing increments over time as well. In fig. 5.3 the population ratio of the two levels are plotted with respect to the recombiner phase. The effect of the quasi-momentum and - comparing both figures - the effect of a higher step counts $T$ as well can be studied.

The influence of the quasimomentum is strongest where the population transfer to ideally only one level occurs, i.e. $\chi = n\pi$ with $n = -1, 0, 1$. The purity of the population

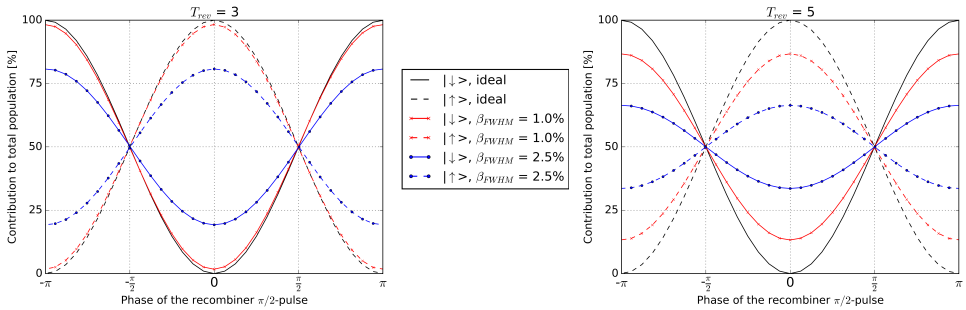


**(a)** Reversing after $T = 3$ **(b)** Reversing after $T = 5$

**Figure 5.3.:** Population of each internal level in dependency of the recombiner phase $\chi$ for $k = 1.5$.

transfer at $\chi = 0$ is plotted over the width in quasimomentum in fig. 5.4.

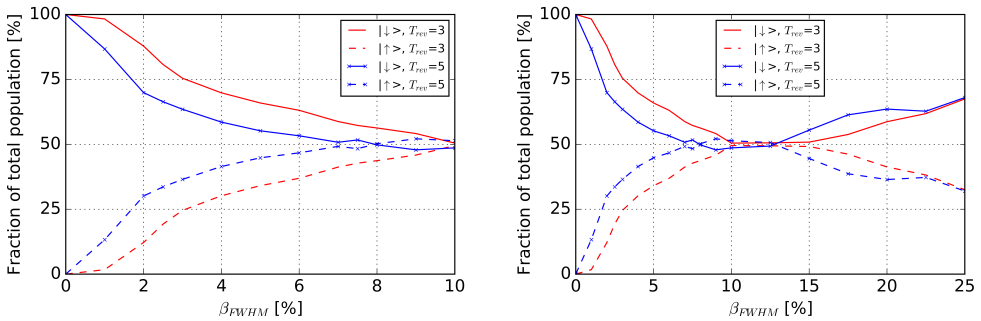


**Figure 5.4.:** The population of a single internal level as a measure of the purity of the population transfer at $\chi = 0$. A higher width in quasimomentum quickly decreases the level separation. For even higher widths the purity rises back a bit.

As expected from fig. 5.3 the purity of the level separation quickly drops if dephasing due to the quasimomentum is taken into account. For a width of about 10% this steadily decreases until no population transer is visible any more. This however rises once more for even higher widths in quasimomentum. At the current setting of $\beta_{FWHM}$ determining the purity of the population transfer for $\chi = 0$ allows a more precise measurement of the width in the BEC.

# 6. Conclusion

## Summary

Motivated by an ongoing experimental time-discrete quantum walk scheme [16, 37], we are interested in the study of the experimental limitations for the walk. These namely are the quasi-momentum $\beta$, influencing the free evolution between two consecutive kicks, and the thermal cloud around the prepared BEC in the experiment. We furthermore compared the simulations including the mentioned influences with the experimental results for different walk applications such as steered walks or the transition to classical behaviour due to noise.
In the last chapter we examined a probable walk reversal but switched to reversing the ratchet currents as a walk reversal is not implementable with the given experimental setting at the moment.

A theory was developed to include the near-resonant quasi-momenta into the analytical expressions for the momentum distributions of the quantum walk. The approach was different to the one applied for the atom optics kicked rotor in [23] in order to include the mixing of the internal levels. With the help of an approximation valid for the near-resonant case $\beta \approx 0$ an expression was found that could be interpreted in analogy with the quantum walk along a Galton board structure [31].
An analytical expression for the resonant case, i.e. $\beta = 0$, was already given in [17] but was rather abstract and unintuitive. The two analytical expression were shown to be identical in quantum resonance.

As the walk becomes experimentally stable for a larger number of kicks up to 20 steps in this thesis we were also able to check the quantum walk theory by running simulations parallely to the experimental results. A good agreement was found in the parameter match together with similar momentum distributions. Including effects like the thermal cloud could furthermore improve the agreement. It is also possible to steer the walk using either biased coins or kicking strengths and thus breaking the symmtery of the walk. Another topic investigated is the transition from pure quantum behaviour to classical one. In this case the phase of the microwave mixing the internal levels is randomized around its ideal value. Increasing the window for the offset phase leads to a transition to classical behaviour and for a totally random phase the classical Gaussian distribution can be obtained.

In the last section an experimentally accessible scheme for a probable walk reversal was suggested. Due to the unitarity, the quantum walk is in principle completely reversible.

The biggest obstacle is the free evolution influenced by the near-resonant quasimomenta. The reversal can be simplified by the usage of ratchet currents which - at the current experimental level - make reversals experimentally feasable. We note that this is no quantum walk reversal anymore because the crucial mixing part is omitted here. The quasimomentum leads to a less pure population separation which depends on the width of its corresponding distribution.

## Outlook

Even though we focussed on the two essential effects impacting on the walk, further aspects might be interesting to investigate in future studies.

The developed analytic expressions for the momentum distributions do not include the far-off-resonant quasi-momenta which would be needed to analytically investigate the effect of the thermal cloud. It can be seen as an ensemble of particles mostly with off-resonant quasi-momenta. On the other hand, even small deviations from the quantum resonance can lead to high dephasing over a few dozen walk steps. This is why the approximation in this thesis fails for higher walk steps and it is therefore needed to find an analytical expression for a bigger range of quasi-momenta.
It is also interesting to include biased coins or kicking strengths into the theory. The latter is especially relevant in the experiment as the laser intensity and therefore the kicking strengths seem to drift away from the desired strength. This could furthermore connect the quantum walk to previous works on steered walks [43].

From an experimental viewpoint, the implemented walk has the advantage of being steerable in direction as well in its transition to classical behaviour. The experimental data showed the same behaviour as we had predicted via simulations. That is why this implemented quantum walk is especially useful in future quantum algorithms [2].
The proposed walk could even be extended to higher walk dimensions but with some caveats. The used optical lattice is indeed easily extendable into a two-dimensional one. However, this raises the problem that the BEC atoms at each lattice site expand two-dimensionally and each particle might feel varying kick strengths as they are not spatially confined enough. It is also not clear on how to connect the perpendicular grid with each other. This connection is crucial for correlated walks and the main interesting feature of probable multi-dimensional walks [44, 45, 46].
A different approach is to superimpose two momentum grids with different spacing, e.g. the second grid could only consist of even momentum classes. The connection could be made by the spacing ratio of the two grids. A walk step on one grid would have effects on the other one and the impact of this intertwining is an open question so far.

Investigating the ratchet reversal might furthermore open the possibility of measuring the width in quasi-momentum in a possible matter-wave interferometer set-up. It is of interest how this set-up extends to the quantum walk reversal and responds to its variations, such as reversed biased walks. This gives more insight into the relation

between the quantum walks and its governing parameters like kick strengths or coin choices.

# A. Useful relations for Bessel functions of the first kind

Mathematically, Bessel functions of the first kind are solutions to the differential equation

$$z^2 \frac{\mathrm{d}^2 f}{\mathrm{d}z^2} + z \frac{\mathrm{d}f}{\mathrm{d}z} + \left(z^2 - n^2\right) f = 0 \tag{A.1}$$

but are also of physical interest when working with the atom optics kicked rotor of section 1.1. The following formulas are intended to give an overview of probably useful relations for further studies. Eqs. A.7, A.9 & A.10 are used in chapter 2.

From chapter 2·1.2[1], *recurrence relations*:

$$J_{n-1}(z) + J_{n+1}(z) = \frac{2n}{z}\, J_n(z) \qquad [1] \tag{A.2}$$

$$J_{n-1}(z) - J_{n+1}(z) = 2\frac{d}{dz} J_n(z) \qquad [2] \tag{A.3}$$

$$\frac{d}{dz}\left(z^n J_n(z)\right) = z^n J_{n-1}(z) \qquad [5] \tag{A.4}$$

From chapter 2·2.2:

$$1 = \sum_{n \in \mathbb{N}_0} \epsilon_{2n}\, J_{2n}(z) \text{ with } \epsilon_n = 2 - \delta_{n,0} \qquad [7] \tag{A.5}$$

$$z = \sum_{n \in \mathbb{N}_0} \epsilon_{2n+1}\, (2n+1) J_{2n+1}(z) \qquad [8] \tag{A.6}$$

From chapter 2·4, *addition rules*:

$$J_n(y+z) = \sum_{r \in \mathbb{Z}} J_r(z) J_{n-r}(y) \qquad [1] \tag{A.7}$$

From chapter 2·7.2:

$$z^2 = \frac{1}{2} \sum_{n \in \mathbb{N}} \epsilon_n\, 4n^2 J_n^2(z) \qquad [3] \tag{A.8}$$

[1] All formulas are taken from [41] with indicated chapter and the respective enumeration given in brackets [ ]

From chapter 3·6.2:

$$J_n\left(z \cdot e^{l\pi i}\right) = e^{ln\pi i} J_n(z) \qquad l \in \mathbb{Z} \qquad [1] \qquad \text{(A.9)}$$

$$J_{-n}\left(z \cdot e^{l\pi i}\right) = e^{-ln\pi i} J_{-n}(z) \qquad [2] \qquad \text{(A.10)}$$

From chapter 5·3, *further addition rules*:

$$J_n(y - z) = \sum_{r \in \mathbb{Z}} J_r(z) J_{n+r}(y) \qquad [4] \qquad \text{(A.11)}$$

$$J_{-n}(y + z) = \sum_{r \in \mathbb{Z}} (-1)^r J_r(z) J_{-n+r}(y) \qquad [4] \qquad \text{(A.12)}$$

From chapter 11·2, *Parseval's integral*[2] *and Neumann's addition theorem*:

$$J_0(z) = \frac{1}{2\pi} \int_{-\pi}^{\pi} e^{iz\cos(\theta)} \mathrm{d}\theta = \frac{1}{2\pi} \int_{-\pi}^{\pi} e^{iz\cos(\theta - a)} \mathrm{d}\theta \quad \forall z \in \mathbb{C}, \forall a \in \mathbb{R} \qquad \text{(A.13)}$$

$$J_0\left(\sqrt{Z^2 + z^2 - 2Zz\cos(\phi)}\right) = \sum_{n \in \mathbb{Z}} \epsilon_n J_n(Z) J_n(z) \cos(n\phi) \qquad [1] \qquad \text{(A.14)}$$

The last following approximation for large $n$ is taken from [40] missing above:

$$J_n(z) \sim \frac{1}{\sqrt{2\pi n}} \left(\frac{ez}{2n}\right)^n \qquad [9.3.1] \qquad \text{(A.15)}$$

[2] Not numerated

# B. Step-wise calculations of the respective matrix elements

## T=1 and 2

$$\hat{U}_{kick} = \hat{M}\cdot\hat{F}\cdot\hat{K} = \frac{1}{\sqrt{2}}\begin{pmatrix}1 & i\\ i & 1\end{pmatrix} e^{-i\tau\beta\hat{n}} \begin{pmatrix} e^{-ik\cos(\hat{\theta})} & 0\\ 0 & e^{ik\cos(\hat{\theta})}\end{pmatrix} \tag{B.1}$$

$$= \frac{1}{\sqrt{2}} e^{-i\tau\beta\hat{n}} \begin{pmatrix} e^{-ik\cos(\hat{\theta})} & ie^{ik\cos(\hat{\theta})}\\ ie^{-ik\cos(\hat{\theta})} & e^{ik\cos(\hat{\theta})}\end{pmatrix} \tag{B.2}$$

$$= \frac{1}{\sqrt{2}} e^{-i\tau\beta\hat{n}} \sum_m i^m J_m(k) e^{im\hat{\theta}} \begin{pmatrix} (-1)^m & i\\ i(-1)^m & 1\end{pmatrix} \tag{B.3}$$

$$= \frac{1}{\sqrt{2}} \sum_m i^m J_m(k) e^{-i\tau\beta\hat{n}} \sum_j |j+m\rangle\langle j| \begin{pmatrix} (-1)^m & i\\ i(-1)^m & 1\end{pmatrix} \tag{B.4}$$

$$= \frac{1}{\sqrt{2}} \sum_m i^m J_m(k) \sum_j e^{-i\tau\beta(j+m)} |j+m\rangle\langle j| \begin{pmatrix} (-1)^m & i\\ i(-1)^m & 1\end{pmatrix} \tag{B.5}$$

$$\hat{U}^2_{kick} = \left[\frac{1}{\sqrt{2}}\begin{pmatrix}1 & i\\ i & 1\end{pmatrix} e^{-i\tau\beta\hat{n}} \begin{pmatrix} e^{-ik\cos(\hat{\theta})} & 0\\ 0 & e^{ik\cos(\hat{\theta})}\end{pmatrix}\right]^2 \tag{B.6}$$

$$= \frac{e^{-i\tau\beta\hat{n}}}{\sqrt{2}^2} \sum_{m_2,m_1} i^{m_1+m_2} J_{m_1}(k) J_{m_2}(k) \sum_{j',j} e^{-i\tau\beta(j+m_1)}$$
$$\times |j'+m_2\rangle \underbrace{\langle j'|j+m_1\rangle}_{=\delta_{j',j+m_1}} \langle j| \begin{pmatrix} (-1)^{m_2} & i\\ i(-1)^{m_2} & 1\end{pmatrix} \begin{pmatrix} (-1)^{m_1} & i\\ i(-1)^{m_1} & 1\end{pmatrix} \tag{B.7}$$

$$= \frac{1}{\sqrt{2}^2} \sum_{m_2,m_1} i^{m_1+m_2} J_{m_1}(k) J_{m_2}(k) \sum_j e^{-i\tau\beta(2j+2m_1+m_2)} |j+m_1+m_2\rangle\langle j|$$
$$\times \begin{pmatrix} (-1)^{m_1}\left[(-1)^{m_2}-1\right] & i\left[(-1)^{m_2}+1\right]\\ i(-1)^{m_1}\left[(-1)^{m_2}+1\right] & -\left[(-1)^{m_2}-1\right]\end{pmatrix} \tag{B.8}$$

## Proof of the recurrence

The start of the proof by induction is already given in B.5. Doing the induction step $T \mapsto T+1$

$$\begin{aligned}
\hat{U}_{kick}^{T+1} =& \left[\frac{1}{\sqrt{2}} \sum_{m_{T+1}} i^{m_{T+1}} J_{m_{T+1}}(k) \sum_{j'} e^{-i\tau\beta\hat{n}} \left|j' + m_{T+1}\right\rangle\!\left\langle j'\right| \begin{pmatrix} \cdots \end{pmatrix}\right] \cdot \hat{U}_{kick}^{T} \\
=& \frac{1}{\sqrt{2}^{T+1}} \sum_{m_1,\ldots,m_{T+1}} i^{\sum_{i=1}^{T} m_i} \left(\prod_{i=1}^{T} J_{m_i}(k)\right) i^{m_{T+1}} J_{m_{T+1}}(k) \\
& \times \sum_{j',j} e^{-i\tau\beta\hat{n}} e^{-i\tau\beta\left(Tj+\sum_{i=1}^{T}(T+1-i)m_i\right)} \left|j' + m_{T+1}\right\rangle \underbrace{\left\langle j' \middle| j + \sum_{i=1}^{T} m_i \right\rangle}_{=\delta_{j',j+\sum_{i=1}^{T} m_i}} \left\langle j\right| RM_{T+1} \\
=& \frac{1}{\sqrt{2}^{T+1}} \sum_{m_1,\ldots,m_{T+1}} i^{\sum_{i=1}^{T+1} m_i} \left(\prod_{i=1}^{T+1} J_{m_i}(k)\right) \sum_{j} e^{-i\tau\beta\left(j+\sum_{i=1}^{T+1} m_i\right)} \\
& \times e^{-i\tau\beta\left(Tj+\sum_{i=1}^{T}(T+1-i)m_i\right)} \left| j + \sum_{i=1}^{T+1} m_i \right\rangle\!\left\langle j \right| RM_{T+1} \\
=& \frac{1}{\sqrt{2}^{T+1}} \sum_{m_1,\ldots,m_{T+1}} i^{\sum_{i=1}^{T+1} m_i} \left(\prod_{i=1}^{T+1} J_{m_i}(k)\right) \\
& \times \sum_{j} e^{-i\tau\beta\left((T+1)j+\sum_{i=1}^{T+1}(T+2-i)m_i\right)} \left| j + \sum_{i=1}^{T+1} m_i \right\rangle\!\left\langle j \right| RM_{T+1}
\end{aligned} \tag{B.9}$$

□

The recurrence of the matrix $RM_T$ is shown via

$$\begin{aligned}
RM_{T+1} =& \begin{pmatrix} (-1)^{m_{T+1}} & i \\ i(-1)^{m_{T+1}} & 1 \end{pmatrix} \cdot RM_T \\
=& \begin{pmatrix} (-1)^{m_1}\left[(-1)^{m_{T+1}} A_T - (-1)^{m_{T+1}} - \tilde{A}_T - 1\right] & i\left[(-1)^{m_{T+1}} B_T + (-1)^{m_{T+1}} - \tilde{B}_T + 1\right] \\ i(-1)^{m_1}\left[(-1)^{m_{T+1}} A_T - (-1)^{m_{T+1}} + \tilde{A}_T + 1\right] & -\left[(-1)^{m_{T+1}} B_T + (-1)^{m_{T+1}} + \tilde{B}_T - 1\right] \end{pmatrix}
\end{aligned} \tag{B.10}$$

giving

$$\begin{aligned}
A_{T+1} &= (-1)^{m_{T+1}} A_T - (-1)^{m_{T+1}} - \tilde{A}_T & B_{T+1} &= (-1)^{m_{T+1}} B_T + (-1)^{m_{T+1}} - \tilde{B}_T \\
\tilde{A}_{T+1} &= (-1)^{m_{T+1}} A_T - (-1)^{m_{T+1}} + \tilde{A}_T & \tilde{B}_{T+1} &= (-1)^{m_{T+1}} B_T + (-1)^{m_{T+1}} + \tilde{B}_T
\end{aligned} \tag{B.11}$$

## Calculation of the momentum distribution

### T=1

The calculation here is rather straight-forward:

$$\begin{aligned}
\left\langle n\uparrow\middle|\hat{U}_{kick}\middle|\varphi_0\right\rangle =& \langle n|\begin{pmatrix}1 & 0\end{pmatrix}\frac{1}{\sqrt{2}}\sum_m i^m J_m(k)\sum_j e^{-i\tau\beta(j+m)}\,|j+m\rangle\langle j| \\
&\times RM_1\cdot\frac{1}{N}\sum_l(-i)^l\,|l\rangle\begin{pmatrix}1\\1\end{pmatrix} && \text{(B.12)}\\
=&\frac{1}{\sqrt{2}N}\sum_m i^m J_m(k)\left[(-1)^m+i\right]\sum_j e^{-i\tau\beta(j+m)} \\
&\times\sum_l(-i)^l\,\langle n|j+m\rangle\underbrace{\langle j|l\rangle}_{=\delta_{j,l}} && \text{(B.13)}\\
=&\frac{1}{\sqrt{2}N}\sum_m i^m J_m(k)\left[(-1)^m+i\right]\sum_l e^{-i\tau\beta(l+m)}(-i)^l\underbrace{\langle n|l+m\rangle}_{\substack{=\delta_{m,n-l}\\=\delta_{n,l+m}}} && \text{(B.14)}\\
=&\frac{1}{\sqrt{2}N}\sum_l i^{n-l}(-i)^l e^{-i\tau\beta n}J_{n-l}(k)\left[(-1)^{n-l}+i\right] && \text{(B.15)}\\
=&\frac{i^n e^{-i\tau\beta n}}{\sqrt{2}N}\sum_l(-1)^l\left[(-1)^{n-l}J_{n-l}(k)+iJ_{n-l}(k)\right] && \text{(B.16)}\\
=&\frac{i^n e^{-i\tau\beta n}}{\sqrt{2}N}\sum_l(-1)^l\left[J_{n-l}(-k)+iJ_{n-l}(k)\right] && \text{(B.17)}\\
\left\langle n\downarrow\middle|\hat{U}_{kick}\middle|\varphi_0\right\rangle =&\frac{1}{\sqrt{2}N}\sum_l i^{n-l}(-i)^l e^{-i\tau\beta n}J_{n-l}(k)\left[i(-1)^{n-l}+1\right] && \text{(B.18)}\\
=&\frac{i^n e^{-i\tau\beta n}}{\sqrt{2}N}\sum_l(-1)^l\left[iJ_{n-l}(-k)+J_{n-l}(k)\right] && \text{(B.19)}
\end{aligned}$$

yielding

$$\left|\left\langle n\downarrow\middle|\hat{U}_{kick}\middle|\varphi_0\right\rangle\right|^2=\frac{1}{2N^2}\left|\sum_l(-1)^l\left[iJ_{n-l}(-k)+J_{n-l}(k)\right]\right|^2 \qquad \text{(B.20)}$$

$$\left|\left\langle n\uparrow\middle|\hat{U}_{kick}\middle|\varphi_0\right\rangle\right|^2=\frac{1}{2N^2}\left|\sum_l(-1)^l\left[J_{n-l}(-k)+iJ_{n-l}(k)\right]\right|^2 \qquad \text{(B.21)}$$

A similar result as before is desired to obtain for a higher kick count and - with the described approximation - is achieved in the following.

**T=2**

$$\left\langle n\uparrow\middle|\hat{U}_{kick}^{2}\middle|\varphi_0\right\rangle = \langle n|\begin{pmatrix}1 & 0\end{pmatrix}\frac{1}{2}\sum_{m_1,m_2} i^{m_1+m_2}J_{m_1}(k)J_{m_2}(k)e^{-i\tau\beta(2j+2m_1+m_2)} \times \sum_j |j+m_1+m_2\rangle\langle j|\, RM_2\cdot\frac{1}{N}\sum_l(-i)^l\,|l\rangle\begin{pmatrix}1\\1\end{pmatrix} \tag{B.22}$$

$$= \frac{1}{2N}\sum_{m_1,m_2} i^{m_1+m_2}\,(*\uparrow)_2\,J_{m_1}(k)J_{m_2}(k)e^{-i\tau\beta(2j+2m_1+m_2)} \times \sum_j \langle n|j+m_1+m_2\rangle\cdot\sum_l(-i)^l\,\langle j|l\rangle \tag{B.23}$$

where $(*\uparrow)_2$ denotes the sum of the two upper matrix elements in eq. B.8 and is abbreviated for short-hand notations.

$$\left\langle n\uparrow\middle|\hat{U}_{kick}^{2}\middle|\varphi_0\right\rangle = \frac{1}{2N}\sum_{m_1,m_2} i^{m_1+m_2}\,(*\uparrow)_2\,J_{m_1}(k)J_{m_2}(k)e^{-i\tau\beta(2l+2m_1+m_2)} \times \sum_l(-i)^l\underbrace{\langle n|l+m_1+m_2\rangle}_{\substack{=\delta_{n-l,m_1+m_2}\\=\delta_{m_2,n-l-m_1}}} \tag{B.24}$$

$$= \frac{1}{2N}\sum_l i^{n-l}(-i)^l\sum_{m_1}(*\uparrow)_2\Big|_{m_2=n-l-m_1} \times J_{m_1}(k)J_{n-l-m_1}(k)e^{-i\tau\beta(2l+m_1+n-l)} \tag{B.25}$$

$$= \frac{i^n e^{-i\tau\beta n}}{2N}\sum_l(-1)^l e^{-i\tau\beta l}\sum_{m_1}(*\uparrow)_2\Big|_{m_2=n-l-m_1} \times J_{m_1}(k)J_{n-l-m_1}(k)e^{-i\tau\beta m_1} \tag{B.26}$$

The approximation results in

$$\left\langle n\uparrow\middle|\hat{U}_{kick}^{2}\middle|\varphi_0\right\rangle \approx \frac{i^n e^{-i\tau\beta n}}{2N}\sum_l(-1)^l e^{-i\tau\beta l}\sum_{m_1}(*\uparrow)_2\Big|_{m_2=n-l-m_1} \times J_{m_1}(k\cdot e^{-i\tau\beta})J_{n-l-m_1}(k) \tag{B.27}$$

$$= \frac{i^n e^{-i\tau\beta n}}{2N}\sum_l(-1)^l e^{-i\tau\beta l}\sum_m J_m(k\cdot e^{-i\tau\beta})J_{n-l-m}(k) \times\left(\left[(-1)^{n-l}-(-1)^m\right]+i\left[(-1)^{n-l-m}+1\right]\right) \tag{B.28}$$

$$
\begin{aligned}
=&\frac{i^n e^{-i\tau\beta n}}{2N}\sum_l (-1)^l e^{-i\tau\beta l} \\
&\times\Bigg[(-1)^{n-l}\sum_m J_m(k\cdot e^{-i\tau\beta})J_{n-l-m}(k)-\sum_m J_m(-k\cdot e^{-i\tau\beta})J_{n-l-m}(k) \\
&\quad +i\sum_m J_m(k\cdot e^{-i\tau\beta})J_{n-l-m}(-k)+i\sum_m J_m(k\cdot e^{-i\tau\beta})J_{n-l-m}(k)\Bigg]
\end{aligned}
\tag{B.29}
$$

$$
\begin{aligned}
=&\frac{i^n e^{-i\tau\beta n}}{2N}\sum_l (-1)^l e^{-i\tau\beta l}\left[(-1)^{n-l}J_{n-l}\left[k\left(1+e^{-i\tau\beta}\right)\right]-J_{n-l}\left[k\left(1-e^{-i\tau\beta}\right)\right]\right. \\
&\left.+iJ_{n-l}\left[k\left(e^{-i\tau\beta}-1\right)\right]+iJ_{n-l}\left[k\left(1+e^{-i\tau\beta}\right)\right]\right]
\end{aligned}
\tag{B.30}
$$

$$
\begin{aligned}
=&\frac{i^n e^{-i\tau\beta n}}{2N}\sum_l (-1)^l e^{-i\tau\beta l}\left[J_{n-l}\left[-k\left(1+e^{-i\tau\beta}\right)\right]-J_{n-l}\left[k\left(1-e^{-i\tau\beta}\right)\right]\right. \\
&\left.+iJ_{n-l}\left[k\left(e^{-i\tau\beta}-1\right)\right]+iJ_{n-l}\left[k\left(1+e^{-i\tau\beta}\right)\right]\right]
\end{aligned}
\tag{B.31}
$$

yielding (analogously for the other internal level)

$$
\begin{aligned}
\left|\left\langle n\uparrow\middle|\hat{U}_{kick}^2\middle|\varphi_0\right\rangle\right|^2 \approx&\frac{1}{4N^2}\left|\sum_l (-1)^l e^{-i\tau\beta l}\left(J_{n-l}\left[-k\left(1+e^{-i\tau\beta}\right)\right]\right.\right. \\
&-J_{n-l}\left[k\left(1-e^{-i\tau\beta}\right)\right]+iJ_{n-l}\left[k\left(e^{-i\tau\beta}-1\right)\right] \\
&\left.\left.+iJ_{n-l}\left[k\left(1+e^{-i\tau\beta}\right)\right]\right)\right|^2
\end{aligned}
\tag{B.32}
$$

$$
\begin{aligned}
\left|\left\langle n\downarrow\middle|\hat{U}_{kick}^2\middle|\varphi_0\right\rangle\right|^2 \approx&\frac{1}{4N^2}\left|\sum_l (-1)^l e^{-i\tau\beta l}\left(iJ_{n-l}\left[-k\left(1+e^{-i\tau\beta}\right)\right]\right.\right. \\
&+iJ_{n-l}\left[k\left(1-e^{-i\tau\beta}\right)\right]-J_{n-l}\left[k\left(e^{-i\tau\beta}-1\right)\right] \\
&\left.\left.+J_{n-l}\left[k\left(1+e^{-i\tau\beta}\right)\right]\right)\right|^2
\end{aligned}
\tag{B.33}
$$

### The general case for T>2

The calculation can be started using eq. 2.11

$$\begin{aligned}
\left\langle n\uparrow\middle|\hat{U}_{kick}^{T}\middle|\varphi_0\right\rangle =& \frac{1}{\sqrt{2}^T N}\sum_{m_1,\ldots,m_T} i^{\sum_{i=1}^{T} m_i}\left(\prod_{i=1}^{T} J_{m_i}(k)\right) \\
& \times \sum_{j,l}(-i)^l e^{-i\tau\beta\left(Tj+\sum_{i=1}^{T}(T+1-i)m_i\right)} \\
& \times \underbrace{\left\langle n\middle| j+\sum_{i=1}^{T} m_i\right\rangle \langle j|l\rangle}_{=\delta_{n-l,\sum m_i}} \begin{pmatrix}1 & 0\end{pmatrix} RM_T \begin{pmatrix}1\\0\end{pmatrix}
\end{aligned} \tag{B.34}$$

$$\begin{aligned}
=& \frac{1}{\sqrt{2}^T N}\sum_{l}\sum_{\substack{m_1,\ldots,m_T \\ \sum m_i=n-l}} i^{n-l}(-i)^l\left(\prod_{i=1}^{T} J_{m_i}(k)\right) \\
& \times e^{-i\tau\beta\left(Tl+\sum_{i=1}^{T}(T+1-i)m_i\right)}\ (*\uparrow)_T\Big|_{\sum m_i=n-l}
\end{aligned} \tag{B.35}$$

$$\begin{aligned}
=& \frac{i^n}{\sqrt{2}^T N}\sum_{l}(-1)^l e^{-i\tau\beta Tl}\sum_{m_1,\ldots,m_{T-1}} e^{-i\tau\beta\sum_{i=1}^{T-1}(T-i)m_i} \\
& \times \left(\prod_{i=1}^{T-2} J_{m_i}(k)\right)\sum_{m_T}\delta_{\sum m_i,n-l} J_{m_{T-1}}(k)\underbrace{J_{m_T}(k)}_{m_T=n-l-m_{T-1}-\sum_{i=1}^{T-2}} \\
& \times \underbrace{e^{-i\tau\beta\sum m_i}}_{=e^{-i\tau\beta(n-l)}}\ (*\uparrow)_T\Big|_{\sum m_i=n-l}
\end{aligned} \tag{B.36}$$

$$\begin{aligned}
=& \frac{i^n e^{-i\tau\beta n}}{\sqrt{2}^T N}\sum_{l}(-1)^l e^{-i\tau\beta(T-1)l}\sum_{m_1,\ldots,m_{T-2}} e^{-i\tau\beta\sum_{i=1}^{T-2}(T-i)m_i} \\
& \times \left(\prod_{i=1}^{T-2} J_{m_i}(k)\right)\sum_{m_{T-1}} J_{m_{T-1}}(k) J_{n-l-\sum_{i=1}^{T-2}-m_{T-1}}(k) \\
& \times e^{-i\tau\beta m_{T-1}}\ (*\uparrow)_T\Big|_{\sum m_i=n-l}
\end{aligned} \tag{B.37}$$

$$\left\langle n \uparrow \middle| \hat{U}_{kick}^{T} \middle| \varphi_0 \right\rangle \approx \frac{i^n e^{-i\tau\beta n}}{\sqrt{2}^T N} \sum_l (-1)^l e^{-i\tau\beta(T-1)l} \sum_{m_1,\ldots,m_{T-2}} \times \left( \prod_{i=1}^{T-2} J_{m_i} \left[ k \cdot e^{-i\tau\beta(T-i)} \right] \right) \sum_{m_{T-1}} J_{m_{T-1}} \left( k \cdot e^{-i\tau\beta} \right) \times J_{n-l-\sum_{i=1}^{T-2} - m_{T-1}}(k) \; (* \uparrow)_T \Big|_{\sum m_i = n-l} \tag{B.38}$$

In the last step, the same approximation was applied as before to allow the application of the addition rule.

# C. Source code example

The implementation using the quantum map was explained in section 4.1. `python 3` allows the allocation of complex valued data types used for the wave functions of the internal levels. In list. C.1 the defined functions for the quantum map are listed. They simulate a walk step by applying the free evolution part of the Floquet operator in eq. 1.12 first. It is followed by the $\delta$-kicking with respective kicking strengths $k1$ and $k2$ (different in sign) which also allows for a steered walk like in chapter 4. Each step is concluded by the instantaneous mixing using eq. 1.23.
For the simulation of the ratchet currents like in section 5.1.2, the same functions can be used, only the mixing is omitted now.
The wave function is initialised following eq. 4.3 but other ratchet states are easily implementable as well. For the simulation of the thermal cloud we consider a Gaussian around momentum class $n = 0$ with $\sigma = 0.5$. As stated in chapter 4.1 the distribution of the quasimomentum follows the same distribution and thus the initial Gaussian wave function is split into an integer momentum class and the quasi-momentum which consists of the fractional part $\in [0, 1)$. The same kicking scheme is imposed on the thermal cloud. The two momentum distributions are blended in together afterwards, since the thermal cloud cannot interact with the BEC. From the experimental data we estimated a fraction of $10 - 15\%$ for the thermal cloud compared to $90 - 85\%$ for the BEC.
As mentioned in section 1.3.3, the spontaneous emission is omitted in the simulations as its impact on the momentum distribution is negligible for up to 20 steps.

```
import numpy as np
import matplotlib.pyplot as plt
from scipy.fftpack import fft, ifft, fftshift, ifftshift

# define the relevant constants
PI = 3.14159265358979323846264338327950288419716939937510582097494459230781641
# source: http://www.pibel.de/
I = complex(0.0,1.0)
E = complex(1.0,0.0)
FWHM_factor = 2.35482004503094938202313865291939927549477137877164107704 5
Tau = 4*PI

############################

def get_norm(psi_vector):
    return np.sum(np.abs(psi_vector)**2)
```

```
def do_kick_evolution(psi, bet, kick,centre):
    if get_norm(psi)==0:
        return psi

    # FFT from momentum into position space
    psi = ifft(psi)
    psi = ifftshift(psi)
    psi *= np.sqrt(2*centre)

    # application of the kick with kick strength
    for i in range(0,2*centre):
        # application of exp(-i*kick*cos(theta))
        theta = 2*PI*i/(2*centre)
        psi[i] *= np.exp(-I*kick*np.cos(theta))

    # Inverse FFT back to momentum space
    psi = ifftshift(psi)
    psi = fft(psi)
    psi /= np.sqrt(2*centre)

    for i in range(0,2*centre):
        # application of exp(-i*tau*(n-n_0)^2/2)
        X = -0.5*Tau*(i-centre+bet)**2
        psi[i] *= np.exp(I*X)

    return psi

def do_mixing(up,down):
    storage = up
    up = (up+I*down)/np.sqrt(2)
    down = (I*storage+down)/np.sqrt(2)
    return up, down

def step_forward(vec_up, vec_down, bet, kick1, kick2,cent):
    # kicking
    vec_up = do_kick_evolution(vec_up, bet, kick1,cent)
    vec_down = do_kick_evolution(vec_down, bet, -kick2,cent)
    # mixing
    for i in range(0,2*cent):
        vec_up[i], vec_down[i] = do_mixing(vec_up[i],vec_down[i])
    return vec_up, vec_down

def calc_prob(up,down,centr):
    P = np.zeros(2*centr)
    for i in range(0,2*centr):
        P_down = np.abs(down[i])**2
        P_up = np.abs(up[i])**2
        P[i] = P_down + P_up
    return P

def preparation(centr):
    up = np.zeros(2*centr,dtype=complex)
    down = np.zeros(2*centr,dtype=complex)
    up[centr] = 0.5
    down[centr] = 0.5
    up[centr+1] = -0.5*I
    down[centr+1] = -0.5*I
    return up, down
```

**Listing C.1:** Defined functions for a basic walk simulation

# List of Figures

# Bibliography


[1] Y. Aharonov, L. Davidovich, and N. Zagury. "Quantum random walks". In: *Phys. Rev. A* 48 (2 1993), pp. 1687–1690. DOI: 10.1103/PhysRevA.48.1687.

[2] N. Shenvi, J. Kempe, and K. B. Whaley. "Quantum random-walk search algorithm". In: *Phys. Rev. A* 67 (5 2003), p. 052307. DOI: 10.1103/PhysRevA.67.052307. URL: https://link.aps.org/doi/10.1103/PhysRevA.67.052307.

[3] A. M. Childs. "Universal Computation by Quantum Walk". In: *Phys. Rev. Lett.* 102 (18 2009), p. 180501. DOI: 10.1103/PhysRevLett.102.180501. URL: http://link.aps.org/doi/10.1103/PhysRevLett.102.180501.

[4] A. M. Childs, D. Gosset, and Z. Webb. "Universal Computation by Multiparticle Quantum Walk". In: *Science* 339.6121 (2013), pp. 791–794. ISSN: 0036-8075. DOI: 10.1126/science.1229957.

[5] M. A. Nielsen and I. L. Chuang. *Quantum computation and quantum information*. Cambridge: University Press, 2000.

[6] M. Karski et al. "Quantum Walk in Position Space with Single Optically Trapped Atoms". In: *Science* 325.5937 (2009), pp. 174–177.

[7] F. Zähringer et al. "Realization of a Quantum Walk with One and Two Trapped Ions". In: *Phys. Rev. Lett.* 104 (10 2010), p. 100503. DOI: 10.1103/PhysRevLett.104.100503. URL: http://link.aps.org/doi/10.1103/PhysRevLett.104.100503.

[8] H. Schmitz et al. "Quantum Walk of a Trapped Ion in Phase Space". In: *Phys. Rev. Lett.* 103 (9 2009), p. 090504. DOI: 10.1103/PhysRevLett.103.090504. URL: http://link.aps.org/doi/10.1103/PhysRevLett.103.090504.

[9] M. A. Broome et al. "Discrete Single-Photon Quantum Walks with Tunable Decoherence". In: *Phys. Rev. Lett.* 104 (15 2010), p. 153602. DOI: 10.1103/PhysRevLett.104.153602. URL: http://link.aps.org/doi/10.1103/PhysRevLett.104.153602.

[10] A. Peruzzo et al. "Quantum Walks of Correlated Photons". In: *Science* 329 (5998 2010), p. 1500.

[11] L. Sansoni et al. "Two-Particle Bosonic-Fermionic Quantum Walk via Integrated Photonics". In: *Phys. Rev. Lett.* 108 (1 2012), p. 010502. DOI: 10.1103/PhysRevLett.108.010502. URL: https://link.aps.org/doi/10.1103/PhysRevLett.108.010502.

[12] T. Kovachy et al. “Quantum superposition at the half-metre scale”. In: *Nature* 528.7583 (Dec. 2015), pp. 530–533.

[13] P. M. Preiss et al. “Strongly correlated quantum walks in optical lattices”. In: *Science* 347.6227 (2015), pp. 1229–1233. DOI: 10.1126/science.1260364.

[14] D. Witthaut. “Quantum walks and quantum simulations with Bloch-oscillating spinor atoms”. In: *Phys. Rev. A* 82 (3 2010), p. 033602. DOI: 10.1103/PhysRevA.82.033602. URL: https://link.aps.org/doi/10.1103/PhysRevA.82.033602.

[15] H. B. Perets et al. “Realization of Quantum Walks with Negligible Decoherence in Waveguide Lattices”. In: *Phys. Rev. Lett.* 100 (17 2008), p. 170506. DOI: 10.1103/PhysRevLett.100.170506. URL: https://link.aps.org/doi/10.1103/PhysRevLett.100.170506.

[16] G. S. Summy and S. Wimberger. “Quantum random walk of a Bose-Einstein condensate in momentum space”. In: *Phys. Rev. A* 93 (2016), p. 023638.

[17] C. Groiseau. “Discrete-Time Quantum Walks in Momentum Space”. MA thesis. University of Heidelberg, 2017.

[18] M. G. Raizen. “Quantum chaos with ultra-cold atoms”. In: *Adv. At. Mol. Opt. Phys.* 41 (1999), p. 43.

[19] J. Ni et al. “Hamiltonian Ratchets with Ultra-Cold Atoms”. In: *Annalen der Physik* 529.8 (2017). 1600335, 1600335–n/a. ISSN: 1521-3889. DOI: 10.1002/andp.201600335. URL: http://dx.doi.org/10.1002/andp.201600335.

[20] S. Wimberger. “Chaos and Localisation: Quantum Transport in Periodically Driven Atomic Systems”. PhD thesis. Ludwig-Maximilians-Universität Munich and Universita degli Studi dell’Insubria, 2004.

[21] F. L. Moore et al. “Atom Optics Realization of the Quantum $\delta$-Kicked Rotor”. In: *Phys. Rev. Lett.* 75.25 (1995), pp. 4598–4601. DOI: 10.1103/PhysRevLett.75.4598.

[22] M. Sadgrove and S. Wimberger. “A pseudo-classical method for the atom-optics kicked rotor: from theory to experiment and back”. In: *Adv. At. Mol. Opt. Phys.* 60 (2011), p. 315.

[23] S. Wimberger, I. Guarneri, and S. Fishman. “Quantum resonances and decoherence for delta-kicked atoms”. In: *Nonlinearity* 16.4 (2003), p. 1381.

[24] F. M. Izrailev. “Simple models of quantum chaos: Spectrum and eigenfunctions”. In: *Physics Reports* 196.5-6 (1990), pp. 299 –392. ISSN: 0370-1573. DOI: 10.1016/0370-1573(90)90067-C.

[25] R. Astumian and M. Bier. “Mechanochemical Coupling of the Motion of Molecular Motors to ATP Hydrolysis”. In: *Physics Today* 55 (2002), p. 33.

[26] M. Sadgrove et al. “Rectified Momentum Transport for a Kicked Bose-Einstein Condensate”. In: *Phys. Rev. Lett.* 99 (4 2007), p. 043002. DOI: 10.1103/PhysRevLett.99.043002.

[27] I. Dana et al. “Experimental Realization of Quantum-Resonance Ratchets at Arbitrary Quasimomenta”. In: *Phys. Rev. Lett.* 100.2 (2008), p. 024103. DOI: 10.1103/PhysRevLett.100.024103.

[28] R. K. Shrestha et al. “Controlling the momentum current of an off-resonant ratchet”. In: *Phys. Rev. A* 86 (4 2012), p. 043617. DOI: 10.1103/PhysRevA.86.043617.

[29] M. Sadgrove and S. Wimberger. “Pseudo-classical theory for directed transport at quantum resonance”. In: *New Journal of Physics* 11.8 (2009), p. 083027.

[30] G. H. Weiss. *Aspects and Applications of the Random Walk*. Amsterdam: North Holland, 1994.

[31] J Kempe. “Quantum random walks: An introductory overview”. In: *Contemporary Physics* 44.4 (2003), pp. 307–327.

[32] A. Ambainis et al. “One-Dimensional Quantum Walks”. In: New York, 2001, pp. 60–69.

[33] A. Steffen et al. “Digital atom interferometer with single particle control on a discretized space-time geometry”. In: *Proceedings of the National Academy of Sciences* 109.25 (2012), pp. 9770–9774. DOI: 10.1073/pnas.1204285109. eprint: http://www.pnas.org/content/109/25/9770.full.pdf. URL: http://www.pnas.org/content/109/25/9770.abstract.

[34] C. S. Hamilton et al. “Driven discrete time quantum walks”. In: *New J. Phys.* 18.7 (2016), p. 073008.

[35] J. Ni et al. “Initial state dependence of a quantum-resonance ratchet”. In: *Phys. Rev. A* 94 (4 2016), p. 043620.

[36] M. Barrett, J. Sauer, and M. Chapman. “All-Optical Formation of an Atomic Bose-Einstein Condensate”. In: *Phys. Rev. Lett.* 87 (1 2001), p. 010404.

[37] S. Dadras et al. *Controlling the directionality and the quantum-to-classical transition of a quantum walk in momentum space*. To be published.

[38] C. Ryu et al. “High-Order Quantum Resonances Observed in a Periodically Kicked Bose-Einstein Condensate”. In: *Phys. Rev. Lett.* 96.16 (2006), p. 160403. DOI: 10.1103/PhysRevLett.96.160403.

[39] J. D. K. Mø lmer Y. Castin. “Monte Carlo wave-function method in quantum optics”. In: *J. Opt. Soc. Am.* B 10 (1993), p. 524.

[40] M. Abramowitz and I. A. Stegun. *Handbook of mathematical functions*. New York: Dover, 1972.

[41] G. N. Watson. *A treatise on the theory of Bessel functions*. Cambridge: University Press, 1922.

[42] With courtesy of Gil Summy and Siamak Dadrasmarani, Oklahoma State University, unpublished work.

[43] M. Weiß et al. “Steering random walks with kicked ultracold atoms”. In: *Phys. Rev. A* 92 (3 2015), p. 033606. DOI: 10.1103/PhysRevA.92.033606.

[44] M. Gräfe et al. “Biphoton generation in quadratic waveguide arrays: A classical optical simulation”. In: *Science* 2 (Aug. 2012), 562 EP –.

[45] K. Poulios et al. “Quantum Walks of Correlated Photon Pairs in Two-Dimensional Waveguide Arrays”. In: *Phys. Rev. Lett.* 112 (14 2014), p. 143604. DOI: 10.1103/PhysRevLett.112.143604. URL: https://link.aps.org/doi/10.1103/PhysRevLett.112.143604.

[46] M. Sadgrove, S. Wimberger, and K. Nakagawa. “Phase-selected momentum transport in ultra-cold atoms”. English. In: *The European Physical Journal D* 66.6, 155 (2012). ISSN: 1434-6060. URL: http://dx.doi.org/10.1140/epjd/e2012-20578-6.

# Erklärung

Ich versichere, dass ich diese Arbeit selbstständig verfasst und keine anderen als die angegebenen Quellen und Hilfsmittel benutzt habe.
Heidelberg, den 4. Dezember 2017,